European Network of Fourier-Transform Ion-Cyclotron-Resonance Mass Spectrometry Centers

Grant Agreement n° 731077

Deliverable D4.3 – Standardized protocol for ultra-high resolution FT-ICR MS measurement

Start date of the project: 1st January 2018
Duration: 60 months
Project Coordinator: Christian ROLANDO – CNRS-
Contact: christian.rolando@univ-lille.fr

"This project has received funding from the European Union's Horizon 2020 research and innovation programme under grant agreement No 731077"

Document Classification

Title	Standardized protocol for ultra-high resolution FT-ICR MS measurement
	P2- LIEG-De Pauw Edwin, P1-Rouen-Carlos Afonso
Work package	WP4- [Insert WP full title]
Dissemination	PU = Public
Nature	R: Document, report
Doc ID Code	20220726_EU_FT-ICR_MS_D4.3
Keywords	Standardized protocols for samples processing

Document History

Name	Date	Comment
2- LIEG-Edwin De Pauw 1-ROUEN-Carlos Afonso	2022-01-10	reformatted

Document Validation

Project Coordinator	Date	E-mail
P1 CNRS – Christian Rolando	2022-07-26	christian.rolando@univ-lille.fr

Neutral Reviewer	Date	E-mail
P1 CNRS – Christian Rolando	2022-07-26	christian.rolando@univ-lille.fr

Document Abstract

Description of optimized protocols for tuning the harmonized cell to its best achievable resolution and extreme mass resolving power MALDI imaging.

Table of Content

1. General Introduction

Standardized protocols are required to obtain reliable results at the optimum operating conditions. Two specific casse are treated, the harmonized cell and MS imaging.

2. Tuning the harmonized cell to its best achievable resolution

Published in **Rapid Communication for Mass Spectrometry** (Rapid Commun. Mass Spectrom.2020, 34, 7, e8659.).

Julien Maillard[1,2], Justine Ferey[2], Christopher P. Rüger[2], Isabelle Schmitz-Afonso[2], Soumeya Bekri[3], Thomas Gautier[1], Nathalie Carrasco[1], Carlos Afonso[2] and Abdellah Tebani[2]

[1] LATMOS/IPSL, Université Versailles St Quentin, UPMC Université Paris 06, CNRS, 11 blvd d'Alembert, F-78280 Guyancourt, France
[2] Université de Rouen, Laboratoire COBRA UMR 6014 & FR 3038, IRCOF, 1 Rue Tesnière, 76821 Mont St Aignan Cedex, France
[3] Department of Metabolic Biochemistry, Rouen University Hospital, Rouen, 76000, France

Abstract

The optimization of the ion trajectories in the ion cyclotron resonance (ICR) cell of a Fourier transform ICR mass spectrometer is a crucial step to obtain the best dynamic range, mass resolution, and mass accuracy. With the recent introduction of the dynamically harmonized cell, the complexity of tuning expanded drastically, and a fine-tuning of the DC voltages is required to optimize the ion cloud movement. This adjustment is typically performed manually.
Here, we propose a computational method based on a design of experiments (DoE) strategy to overcome the limits of classical manual tuning. This DoE strategy was exemplarily applied on a 12T FTICR equipped with a dynamically harmonized ICR cell. The chemometric approach, based on a composite central face design (CCF), was first applied on a reference material (sodium trifluoroacetate) allowing for the evaluation of the primary cell parameters. Eight factors were identified related to shimming and gating. The summed intensity of the signal corresponding to the even harmonics was defined as one quality criteria.
Consequently, the DoE response allowed for rapid and complete mapping of cell parameters resulting in an optimized parameter set. The new set of cell parameters was applied to the study of an ultra-complex sample. Here, Tholins, an ultra-complex mixture that mimics the haze present on Titan, was chosen. We observed a substantial improvement in mass spectrometric performance. The sum of signals related to harmonics was decreased by a factor of three (from 4% for conventional tuning to 1.3%). Furthermore, the dynamic range was also increased and lead to an increase of attributed peaks by 24%.

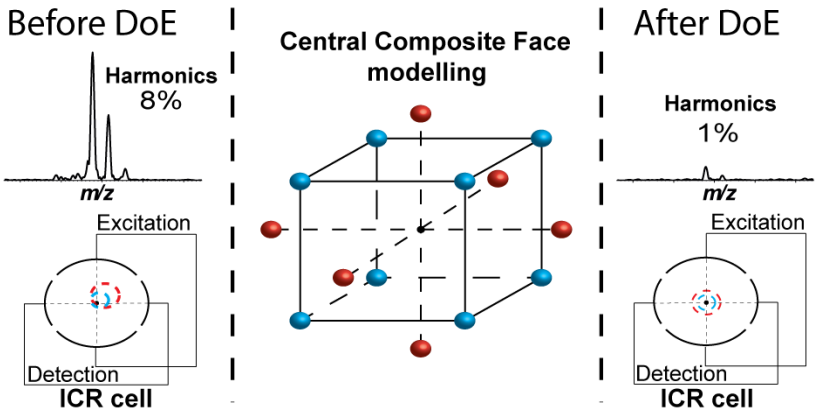

1. Introduction

Fourier Transform Ion Cyclotron Resonance mass spectrometer (FTICR) is well known to be the most powerful mass spectrometer by reaching unprecedented resolving power, mass accuracy and sensitivity levels[1,2]. It turned out to be the most appropriate instrument for the characterization of ultra-complex mixtures such as petroleum[3-7], natural organic matter [8] or extraterrestrial organic matter [9,10]. In order to detect the cyclotron motion, FTICR uses the combination of a static electric field which is hyperbolic near the center and a strong homogeneous static magnetic field (up to 21 Tesla – so far). The combination of both fields retains ions in the cell. Ions in the magnetic field travel according to a cyclotron motion defined by Equation 1.

$$\omega_0 = \frac{qB_0}{m}$$

Equation

In

The

Optimized

In

After

2. Material and methods

2.1.

Tholins

2.2.

2.2.1.

All

For

Complex

2.3.

2.3.1.

DataAnalysis

MODDE

Table

Run	Run	Shi0	Shi90	Gat0	Gat90	SEP
1	10	-	-	-	-	
2	28		-	-	-	-
3	23	-		-	-	-
4	9			-	-	
5	1	-	-		-	-
6	24		-		-	
7	20	-			-	
8	12				-	-
9	29	-	-	-		-
10	8		-	-		
11	6	-		-		
12	5			-		-
13	25	-	-			
14	16		-			-
15	26	-				-
16	17					
17	2	-				
18	13					
19	15		-			
20	19					
21	4			-		
22	14					
23	18				-	
24	22					
25	3					-
26	7					
27	27					
28	31					
29	30					
30	11					
31	21					

2.3.2.

The

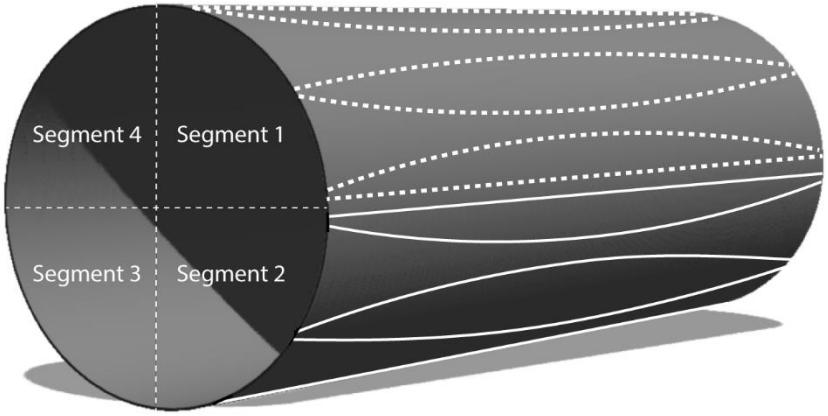

Figure

Parameters

The

Table

Screening

Factor	Intervals	Predicted	Factor
Shim0	1.465	1.535V	15.4
Shim90	1.465	1.540V	33.3
Gat0	1.4	1.620V	12.6
Gat90	1.450	1.550V	10.7
Sweep	20	20%	28.0

Optimization

Factor	Intervals	Predicted	Factor
Shim0	1.530	1.542V	53.1
Shim90	1.530	1.550V	43.4
Gat0	1.600	1.600V	1.9
Gat90	1.540	1.551V	1.7

2.3.3.

Partial

3. Results and discussion

3.1.

The

Figure

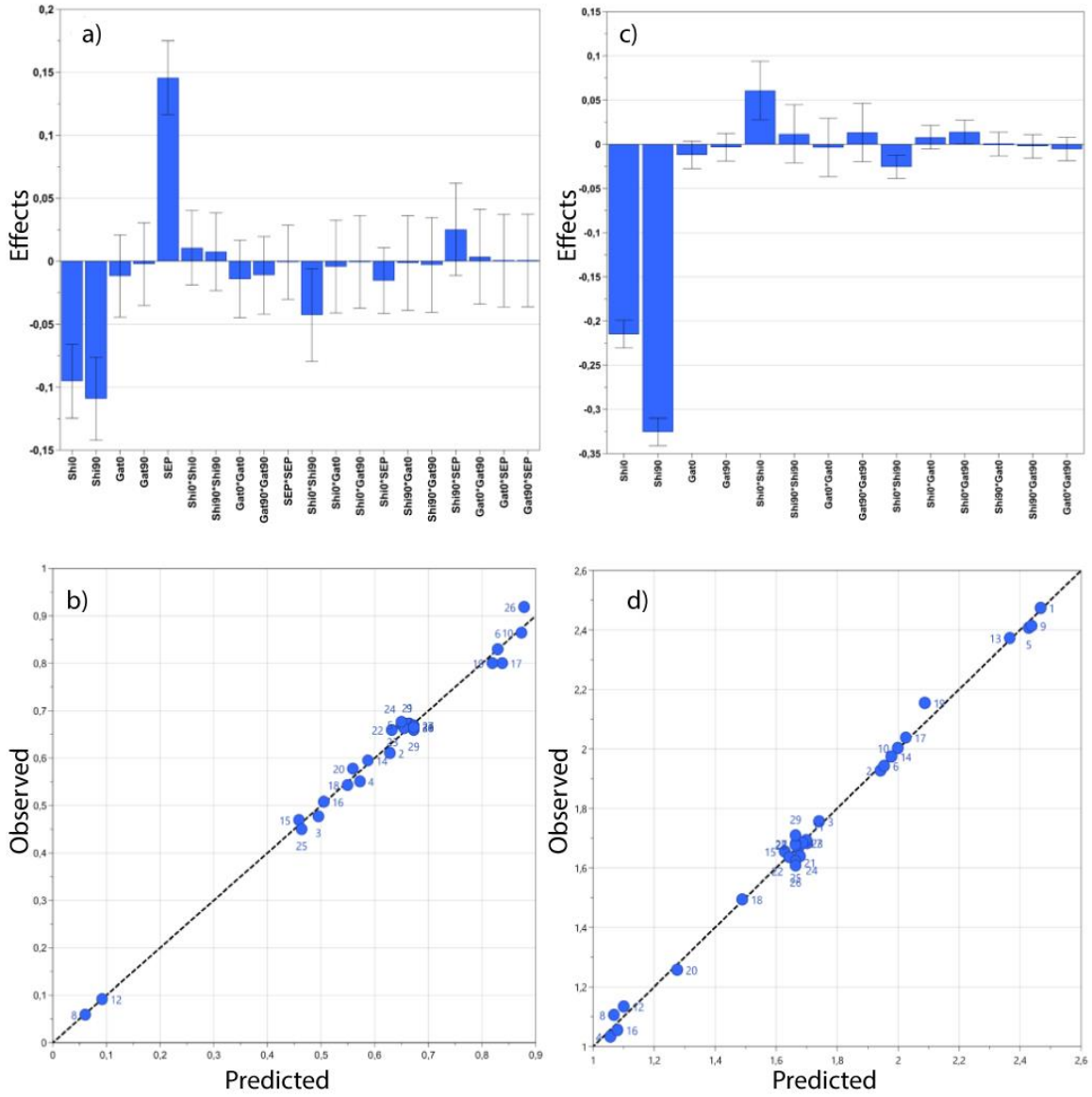

Figure

The

Using

3.2.

As

This

3.3.

The

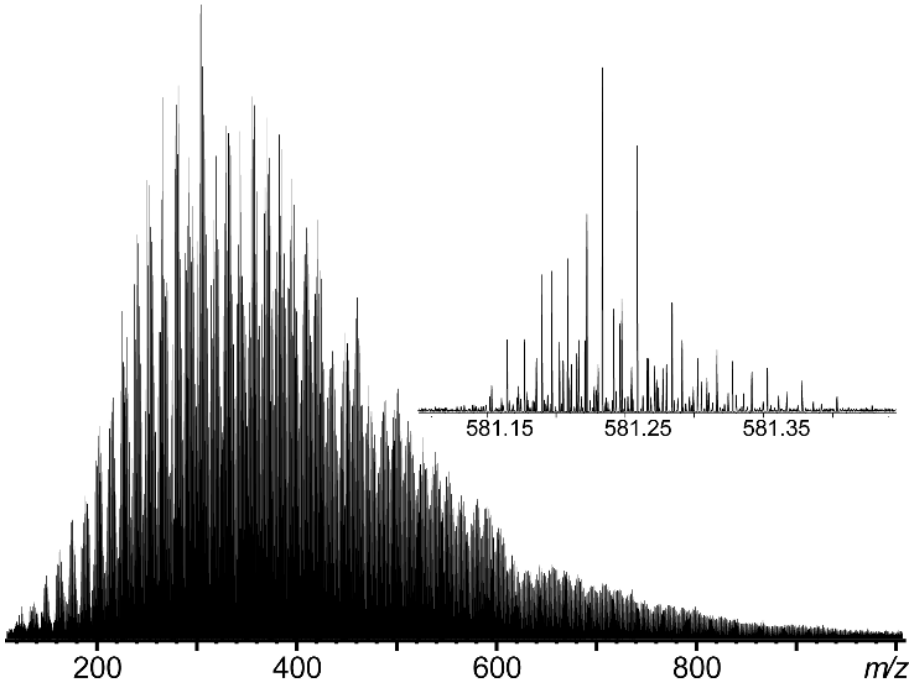

Figure

The

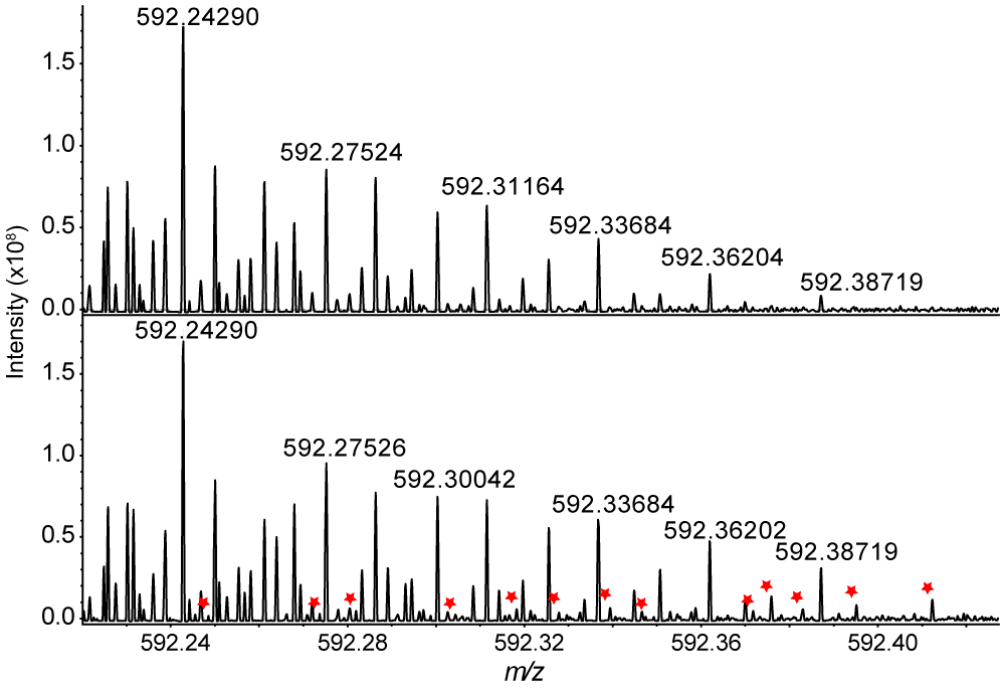

Figure

Different

Table

	Before	Manual	DoE
Attributed	18393	21478	22735
Resolution	1,640,009	1,697,535	1,882,419
RMS	0.13	0.09	0.08
Global	1.2x10E9	1.8x10E9	2.0x10E9

The

4. Conclusion

The

5. Acknowledgments

N.C.

6. References

1.
2.
3.
4.
5.
6.
7.
8.
9.
10.
11.
12.
13.
14.
15.
16.
17.
18.
Umetrics
19.
20.
21.
22.
23.
24.
25.
26.
27.
28.
29.
30.
31.
32.
33.
34.
35.

Supporting

Optimization

Julien

1
2
3

Table
Table
Table
Table
Table
Table

Table S-1: Fractional Factorial design matrix with response values the screening step.

Run N°	Run Order	Shim0 (V)	Shim90 (V)	Gat0 (V)	Gat90 (V)	SEP (%)	Second harmonic (%)
1	10	1.465	1.465	1.400	1.450	40	
2	28	1.535	1.465	1.400	1.450	20	4.083
3	23	1.465	1.540	1.400	1.450	20	2.996
4	9	1.535	1.540	1.400	1.450	40	3.558
5	1	1.465	1.465	1.620	1.450	20	4.694
6	24	1.535	1.465	1.620	1.450	40	6.77
7	20	1.465	1.540	1.620	1.450	40	
8	12	1.535	1.540	1.620	1.450	20	1.143
9	29	1.465	1.465	1.400	1.550	20	4.714
10	8	1.535	1.465	1.400	1.550	40	7.312
11	6	1.465	1.540	1.400	1.550	40	
12	5	1.535	1.540	1.400	1.550	20	1.237
13	25	1.465	1.465	1.620	1.550	40	
14	16	1.535	1.465	1.620	1.550	20	3.937
15	26	1.465	1.540	1.620	1.550	20	2.946
16	17	1.535	1.540	1.620	1.550	40	3.228
17	2	1.465	1.503	1.510	1.500	30	6.332
18	13	1.535	1.503	1.510	1.500	30	3.494
19	15	1.500	1.465	1.510	1.500	30	6.305
20	19	1.500	1.540	1.510	1.500	30	3.788
21	4	1.500	1.503	1.400	1.500	30	4.716
22	14	1.500	1.503	1.620	1.500	30	4.56
23	18	1.500	1.503	1.510	1.450	30	4.599
24	22	1.500	1.503	1.510	1.550	30	4.747
25	3	1.500	1.503	1.510	1.500	20	2.819
26	7	1.500	1.503	1.510	1.500	40	8.281
27	27	1.500	1.503	1.510	1.500	30	4.659
28	31	1.500	1.503	1.510	1.500	30	4.627
29	30	1.500	1.503	1.510	1.500	30	4.567
30	11	1.500	1.503	1.510	1.500	30	4.629
31	21	1.500	1.503	1.510	1.500	30	4.624

Table

Run	Run	Shim0	Shim90	Gat0	Gat90	
1	27	1.530	1.530	1.600	1.540	2.475
2	2	1.550	1.530	1.600	1.540	1.928
3	20	1.530	1.550	1.600	1.540	1.757
4	4	1.550	1.550	1.600	1.540	1.033
5	5	1.530	1.530	1.640	1.540	2.407
6	23	1.550	1.530	1.640	1.540	1.942
7	12	1.530	1.550	1.640	1.540	1.684
8	24	1.550	1.550	1.640	1.540	1.107
9	19	1.530	1.530	1.600	1.570	2.414
10	6	1.550	1.530	1.600	1.570	2.003

11	26	1.530	1.550	1.600	1.570	1.693
12	3	1.550	1.550	1.600	1.570	1.135
13	1	1.530	1.530	1.640	1.570	2.373
14	11	1.550	1.530	1.640	1.570	1.975
15	28	1.530	1.550	1.640	1.570	1.654
16	29	1.550	1.550	1.640	1.570	1.054
17	17	1.530	1.540	1.620	1.555	2.039
18	18	1.550	1.540	1.620	1.555	1.493
19	8	1.540	1.530	1.620	1.555	2.156
20	10	1.540	1.550	1.620	1.555	1.256
21	21	1.540	1.540	1.600	1.555	1.665
22	22	1.540	1.540	1.640	1.555	1.637
23	16	1.540	1.540	1.620	1.540	1.684
24	15	1.540	1.540	1.620	1.570	1.639
25	25	1.540	1.540	1.620	1.555	1.623
26	14	1.540	1.540	1.620	1.555	1.608
27	13	1.540	1.540	1.620	1.555	1.682
28	7	1.540	1.540	1.620	1.555	1.676
29	9	1.540	1.540	1.620	1.555	1.708

Table

Second	Coeff.	Std.	P
Shim0	-	0.01303	0.00049
Shim90	-	0.01455	0.00025
Gat0	-	0.01455	0.64563
Gat90	0.00193	0.01455	0.89872
SEP	0.14123	0.01303	0.00004
Shi0*Shi0	-	0.01310	0.95773
Shi90*Shi90	0.00442	0.01369	0.75791
Gat0*Gat0	-	0.01368	0.47577
Gat90*Gat90	-	0.01368	0.58525
SEP*SEP	0.00569	0.01310	0.67912
Shi0*Shi90	-	0.01633	0.03106
Shi0*Gat0	-	0.01633	0.81987
Shi0*Gat90	-	0.01633	0.97560
Shi0*SEP	-	0.01162	0.18826
Shi90*Gat0	-	0.01669	0.90321
Shi90*Gat90	-	0.01669	0.95099
Shi90*SEP	0.03057	0.01633	0.11029
Gat0*Gat90	0.00019	0.01668	0.99123
Gat0*SEP	-	0.01633	0.98493
Gat90*SEP	0.00031	0.01633	0.98555

N	Q2	0.628		
DF	R2	0.991	RSD	0.03919
Comp.	R2	0.959		

				Confidence	0.95

Table

Second

	DF	**SS**	**MS**	**F**	**p**
Total	27	11.0417	0.40895		
Total	26	0.972344	0.0373979		
Regression	20	0.96313	0.0481565	31.3577	**0**
Residual	6	0.00921428	0.00153571		
	N	Q2	0.628	Cond.	12.05
	DF	R2	0.991	RSD	0.039
	Comp.	R2	0.959		

3. Extreme mass resolving power MALDI imaging

Annexed
FTICR

Published

Mathieu

1
2
3

Abstract

MALDI mass spectrometry imaging (MALDI MSI) is a powerful analytical method providing the 2D localization of compounds from thin sections of typically but not exclusively biological samples. The dynamically harmonized ICR cell (ParaCell©) was recently introduced to achieve extreme spectral resolution capable to provide the isotopic fine structure of ions detected in complex samples. The latest improvement in ICR technology also includes 2ω detection which significantly reduces the transient time while preserving the nominal mass resolving power of the ICR cell. High-resolution MS images acquired on FT-ICR instruments 7T and 9.4T superconducting magnets equipped with the dynamically harmonized ICR cell and operating with the suboptimal parameters, suffered severely from shifting m/z peak from pixel-to-pixel due to space-charge effects. The resulting average mass spectra (or mean spectra) have depreciated mass accuracy and mass resolving power under the instrument specifications which affect the confidence level of the identified ions. Here we propose an analytical workflow based on the monitoring of the Total Ion Current to restrain the shift of m/z peaks from pixel-to-pixel. Optimization of the laser parameters is proposed to maintain high spectral resolution and mass accuracy during MSI analyses within the instrument specifications. The optimized method has been successfully employed in replicates to perform high-quality MALDI MS images at resolving power (FWHM) above 1,000,000 in the lipid mass range across the whole image for superconducting magnets of 9.4T and 7T using 1 and 2ω detection. Our data also compare favorably with MALDI MSI experiments performed on higher magnetic field superconducting magnets, including the 21T MALDI FT-ICR prototype instrument of the NHMFL group at Tallahassee, Florida.

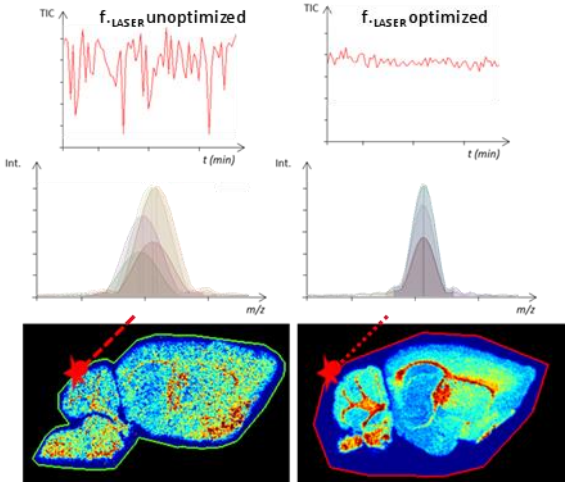

7. Introduction

Matrix-

To

This

8. Material and methods

8.1. Chemicals

Acetone

8.2. Animal handling

Transgenic

Natural

8.3. Tissue sectioning

Mouse

8.4. Matrix coating

Prior

8.5. MALDI mass spectrometry imaging

Mass

Automated

Table

		solariX		scimaX	
Parameters	(Unit)	**Original**	**Re-**	**Original**	**Re-**
Laser	%	98	80	93	85
Laser		600	[2	400	6
Laser	(Hz)	1000	#shots×10	1000	60
Sweep	(%)	22	[16	20	18
Front	(V)	1.5	1.35	3	3.06
Analyzer	(V)	-	-	-	-
Side	(V)	5	[6	0.2	3
Side	(V)	-	-	-	-
Time	(ms)	1.2	1.2	1.0	0.7[b]

a

b

8.6. Data processing

All

9. Results and discussion

Most

A

3.1. Magnetic field and charge-space effects. The determination of the *m/z* ratios by FT-ICR is obtained by converting the rotational frequencies of the ions by Fourier Transform, which depends on the masses and carried charges under the influence of the applied magnetic fields. The space-charge effect limits the performance of FT-ICR due to the influence of the charge repulsion between ion packets if the ICR cell is loaded with more ions than the magnetic field is able to constrain. . Using a superconductive magnet with higher magnetic fields would limit the influence of the space charge effects as explained by Michael

L.Easterling *and coworkers*[34,35] in $\boldsymbol{\omega obs} = \frac{qB}{m} - \frac{2\alpha V}{a^2 B} - \frac{q\rho G_i}{\epsilon_0 B}$ Equation 1, where the unperturbed ion frequency ω_{obs} is the observed frequencies (which are then converted to a mass spectrum), *q* represents the elementary charge magnitude, *B* the magnetic field, *m* the ion mass, *α* the separation between the trapping plates, *V* the voltage difference between upper and side plates, *a* the separation between upper and lower plates, ρ the ion density, G_i the ion cloud geometry and ϵ_0 the void permittivity constant.

$$\boldsymbol{\omega_{obs}} = \frac{qB}{m} - \frac{2\alpha V}{a^2 B} - \frac{q\rho G_i}{\epsilon_0 B} \qquad \textbf{Equation 1}$$

In the space-charge component of the equation ($q\rho G_i$), the importance of ion density and cloud geometry describe how the number of injected ions affects the angular velocity ω and consequently the mass shift observed in the mass spectra. The influence of the magnetic field also restrains the mass shift due to the space-charge component to some extent. In this paper, the main focus is on limiting the ion current fluctuation during the MSI acquisition and restricting the observed mass shift to the extent possible. This corresponds to limiting the fluctuations of the space-charge effect component at constant magnetic field. Nonetheless, the requirement for the magnetic field to produce mass spectrometry images at extreme mass resolving power was evaluated by comparing experimental results from 9.4T to a 7T operated in 1ω and/or 2ω detection modes.

In regard to the theory, our best chance to restrain the experimental mass shift in the average MS images under the specification of the FT-ICR is to prevent the space-charge effects. This was investigated in this work and the literature at different steps of the production of mass spectrometry images, from the sample preparation (matrix deposition protocols) to the instrumental parameters (ion optics transmission and ICR ion optics). Nonetheless the optimization of the settings of the laser parameters are still scarce in the literature and was investigated in this work.

The monitored outputs of the (re)visited experimental parameters during the production of MS images at very high mass resolving power (500'000 and above in the lipid mass range) were mainly the stability of the total ion current (TIC) fluctuation during the image acquisition, the mass resolving power (full width at middle height FWMH) in individual pixel as well as in the average mass spectrum of the image, and the mass shift (i.e. variation of the *m/z* peak apexes from pixel to pixel), as presented in the flowchart [figure 0]. The apparent intrascan dynamic range between major and minor peaks of lipids was also monitored and reported during the laser parameter optimization.

The effect of large fluctuations of TIC values on the shift in *m/z* ratios was first evaluated by monitoring the signal produced by a standard solution of deuterated lipids spotted with α-HCCA matrix on an indium-tin oxide conductive (ITO) glass slide. After the acquisition of a single MALDI-MS scan involving 10 laser shots, the instrument was post-calibrated using the signals from $[PC (15:0/18:1(d7))+H]^+$ *m/z*: 753.613, $[LysoPC (18:1(d7))+H]^+$ *m/z*: 529.399 and $[SM (d18:1/18:1(d9))+H]^+$ *m/z*: 738.647 detected from the deuterated lipids standard solution. The acquired signal was observed with resolutions (FWMH) above 200,000 at their respective *m/z* and MMA better than 0.5ppm (MMA after post-calibration). When the number of injected ions was increased (i.e. using 400 laser shots), it resulted in one order of magnitude higher total ion count injected in the ICR cell and a shifted experimental mass observed for all previously detected ions and MMA now ranging from 2 to 8 ppm. The larger amount of ions introduced into the cell in regards to the calibration procedure severely impaired the mass measurement accuracy. The abrupt modification of the TIC intentionally generated was correlated with the observed mass shift. An example is provided in Figure S1 for illustration based on the signal obtained for $[PC (15:0/18:1(d7))+H]^+$.

From an MSI perspective, such TIC variations commonly appear when inhomogeneous matrix deposition creates hot spots, and/or when samples such as tissue sections are made of regions of interest being intrinsically heterogeneous in terms of molecular compositions and efficiently desorbed/ionized compounds.

3.2. Influence of the sample preparation and the amount of sprayed matrix during laser shots irradiation on the total ion current stabilization. Avoiding the formation of hot-spot due to inhomogeneous deposition of matrix is important to produce MS images of high quality. The KPMP Consortium (Veličković and coworkers), and Tressler and coworkers improved MALDI MSI data after factorial design optimization of the deposited MALDI matrix using an automatic sprayer on mice's kidney tissue sections[24,36]. Here, the amount of deposited MALDI matrix was investigated in terms of signal suppression of the analytes of interest when varying the number of laser shots per pixel is used (see Figure S2). For this purpose, serial sagittal mouse brain slices were prepared with varying amounts of sprayed α-HCCA matrix of 10 and 5 nmol per mm^2 respectively. Mass spectrometry images were acquired either using several hundreds of laser shots at 1000Hz (Figure 1A) or using 6 laser shots at 60Hz (Figure 1B). In the latter case, the laser focus of the solariX XR 9.4T Smartbeam II laser was adjusted from 98% to 80% to ablate and desorb an equivalent amount of material on the matrix-sprayed tissue sections per pixel. This allowed the generation of similar TIC values between the

MALDI MSI methods. Figure 1A shows an unstable TIC for the method employing sub-optimal parameters while the new set of optimized settings showed a drastically improved TIC stability through the entire acquisition (Figure 1B). This resulted in improved alignment of the *m/z* peaks restraining the mass shifts below 0.5 ppm and improved effective mass resolving power in the mean spectrum around 400'000 at *m/z* 400 (Figure 1 A and B panel c) for all the detected ions while keeping the same spatial resolution. An in-house script has been used to monitor the *m/z* channels for every pixel, and compute the distribution of their measured masses (apex of the *m/z* peaks) and the resolving power at half-maximum full width. Figure S3 provides a graphical representation of the mass and resolving power distribution for the ion 782.57 *m/z* ([PE 39:4+H]$^+$ or [PC 36:4+H]$^+$ (according to the LIPID MAPS database) for both methods which were drastically improved when the TIC fluctuation was restrained.

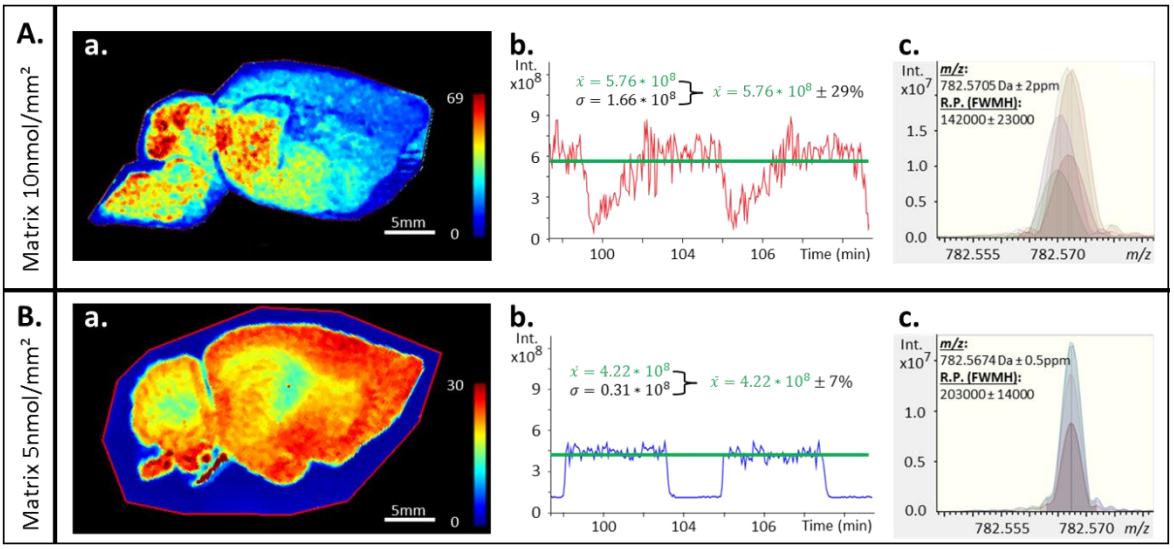

Figure 1. Comparison of dynamically harmonized MALDI-FT-ICR-MSI acquired on a solariX XR 9.4T with manufacturer recommendations-based method (A) and a 6 laser shots-based method (B), see section 3.2 for details. (a) are the reconstructed heat maps of the non-normalized Total Ion Count of MS images. (b) Portions of the TIC over time of MSI acquisition and the computed mean intensities with standard deviation. Observable gaps on the TIC are values from pixels outside of the tissue section and were excluded to compute the standard deviation. Red TIC was obtained when 10nmol/mm² α-HCCA matrix was deposited with 98% laser focus, blue TIC was obtained when 5nmol/mm² α-HCCA matrix was deposited with 80% laser focus (c) Multi-pixel mass spectra overlay of 782.57 *m/z* shows the notable improvement in terms of mass resolving power and mass accuracy measurements during the mass spectrometry images between the unstable (up) and stable (down) Total Ion Count.

3.3. ICR mass analyzer optimization and the influence of ion optic voltages on the TIC stability. Mouse tissue sections were prepared for state-of-the-art mass spectrometry imaging and adapted to the material

available for this work. At first, the method employed was based on the recommended manufacturer MALDI-MS values. Minimal modifications to operate in the 300 to 1200 amu mass range in broadband mode, at theoretical FWMH mass resolving power (R.P.) above 400,000 at m/z 800 with 4M data point were applied. The solariX XR 9.4T instrument was operated following a method optimized by Ferey *and coworkers*[15] . This team optimized the MALDI-FT-ICR MSI parameters using experimental designs of experiments on a 12T magnet instrument fitted with the dynamically harmonized ICR cell. However, our MSI acquisitions performed on our 9.4T magnet suffered from severe mass shifts as shown in Figure 2. For individual pixels of the mass spectrometry image, the experimental R.P. at full-width middle height (FWMH) was slightly above the estimated R.P by the FT-ICR control software (FTMS control). Nevertheless, the centroids of the *m/z* peaks shifted pixel-to-pixel resulting in FWMH and mass accuracy under the specification of our solariX XR 9.4T in the average mass spectrometry image. The MSI mean spectrum showed peaks widening due to the summation of mass spectra of all the MSI pixels. Extreme cases were observed where the spectrum-to-spectrum mass shift was so intense that the *m/z* peaks were splitting by a few milli atomic mass units (i.e. several ppm) as shown in Figure 2d. The reconstructed mass spectrometry image (given a mass tolerance of ±0.004 m/z) of the detected ions (assuming *m/z* 782.57 being $[PC\ 34:1 + Na]^+$ and *m/z* 942.64 being $[CL\ 36:4 + NH_4]^+$ which are ubiquitous lipids) results in biased and incomplete ion distributions unless the targeted ion and its shifted counterpart *m/z* peak (mass tolerance of about ±0.01 m/z) were selected together to reconstruct the MS image (Figure 2e). Comparison of the extracted spectra on a per-pixel basis (Figure 2a) showed that peaks splitting could be linked again to the regions of interest submitted to large TIC variation despite the ion optics optimization adapted from Ferey *and coworkers* for our 9.4T instrument.

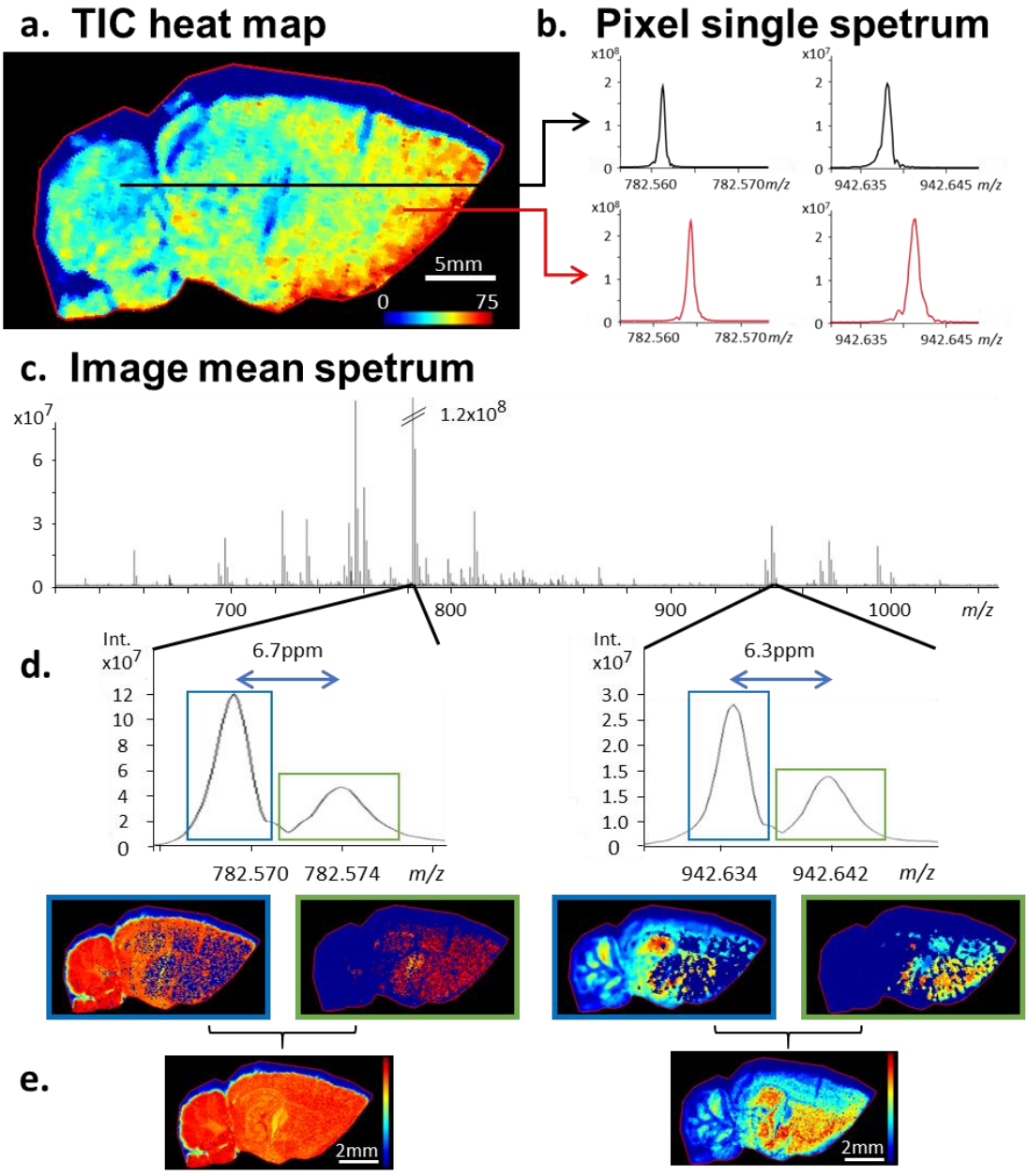

Figure 2. (a) Heat map of the non-normalized Total Ion Current of mouse brain slice MSI analyzed by high-resolution MALDI-FT-ICR-MSI solariX XR 9.4T using non-optimized MSI method. (b) Extracted mass spectra from single pixels located in regions with significant differences in Total Ion Current. (c) Average mass spectrum (mean spectrum) of the whole mass spectrometry image (d) Zoomed mean mass spectrum focused on peaks *m/z* 782.57 *m/z* and 942.64 *m/z* showing artifacts of duplicated peaks and their incomplete distributions due to inconsistent mass measurement accuracy during the MSI acquisition. (e) Obtained localizations with a window selection encompassing both *m/z* peaks shown in the vicinity of *m/z* 782.57 and 942.64 respectively.

Ion optic voltages of the ICR mass analyzer were investigated as options to stabilize the TIC signal (i.e. charge-space effects) in our 9.4T FT-ICR. Thus, investigations were focused on ICR parameters, especially

analyzer entrance, front and back trapping, sidekick, and excitation sweep voltages. Out of those parameters, the sidekick was the only parameter that have a slight influence on the stability of the TIC. The sidekick offset optimization also showed a limited effect on the mass shift, while the front and back trapping, as well as the excitation sweep, affected the peak shapes (as expected) with no effect on the TIC stability. The voltage applied to the analyzer entrance affected the total ion count interestingly. Indeed, an increased analyzer entrance voltage was followed by a gradual decrease of the MS signal. We anticipate that it could potentially be used to limit the introduction of ions inside the ICR cell and act as a real-time ion injection control device. In the end, optimizing the ion optics does not significantly improve the TIC stability during MSI experiments.

3.4. Monitoring MALDI processes and the influence of the number of laser shots. The relationship between the TIC value and the number of laser shots per scan was investigated on mice brain tissue sections. Acquisitions ranging from the minimum number of laser shots per scan up to 600 laser shots on a fixed (x,y) position of the sample were performed. Because acquisitions with a single laser shot resulted in the absence of signal from the tissue and the matrix, 2 laser shots per scan were employed for the minimum number of laser shots per scan. Under this experimental condition, the laser frequency had to be lowered below 300Hz once again due to an absence of signal above this threshold. Below the laser frequency of 300Hz, no significant variations of the MS signal were observed (data not shown). Consequently, for 2 laser shots the laser frequency value was set at 20Hz to easily maintain a ratio of laser shots to laser frequency of 1:10. This ratio also allows for more laser shots to be used to produce MS signal for samples requiring higher laser energy deposition to ionize and desorb the analytes. The range of this laser parameters ratio is then going from 2shots/20Hz to 200shots/2000Hz, where 2000Hz is the operational limit of the Smartbeam II laser of our MALDI ion sources. Setting this ratio keeps the period between laser shots constant, thus balancing the potential effects of the MALDI plume ion extraction efficiency while investigating the effect of the number of laser shots on TIC stability. Beyond 200 laser shots, the maximal laser frequency was used.

Figure 3a shows the TIC accumulation (summed TIC) due to 2 laser shots at 20Hz and Figure 3b shows the TIC value for each scan. Figure 3a indicates that most of the accumulated TIC signal (more than one-half) was obtained from the first 100 laser shots, whereas Figure 3b points out a noticeable instability of the TIC during the 50 first laser shots. The very first shots showed the highest *m/z* peak abundance in the mass spectrum with a relatively high relative abundance (better than 10% relative intensity). The following laser

shots poorly contributed to providing intense *m/z* peaks in the mass spectrum and the less intense *m/z* peaks vanished first. As the laser shots still ablated the same (x,y) sample position, only the most intense peaks observed in the beginning were still detected in the mass spectrum while the other ions were observed close to the noise signals. Figure 3a also shows that the very first laser shots produced a rather linear increase in TIC, followed by a smaller amount of ions produced by subsequent laser shots. Then, a further linear increase is observed after about 120 laser shots due to the accumulation of mainly noise peaks. This result suggests that a smaller amount of laser shots is beneficial to detect the ion with an appropriate signal-to-noise ratio, unless the targeted ions would require a significantly larger amount of laser energy to be detected. Staying within this linear zone should improve the TIC stability pixel-to-pixel and ensure a stable amount of ions injected into the ICR cell, resulting in stable space-charge effects and the production of ultra-high mass resolving power mass spectrometry images. The contribution of the desorption/ionization of the pixel being imaged in terms of time is typically less than 1 second from 2 to 10 laser shots per pixel by operating the laser shot to laser frequency at 1:10 constant ratio.

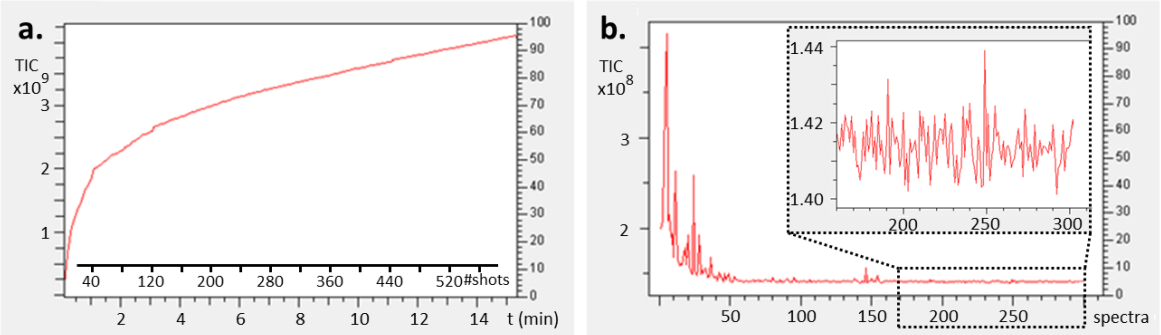

Figure 3. Summed Total Ion Current (TIC accumulation) over time (a) and Total Ion Current per scan (b) for a 300 scans acquisition of 2 laser shots at 20Hz per scan performed on a dynamically harmonized MALDI-FT-ICR solariX XR 9.4T.

3.5. Influence of the laser shots number of the apparent dynamic range of imaged lipids. New sets of mice brain images were produced by MALDI mass spectrometry, varying the number of laser shots at a fixed laser period (i.e. laser shots to laser frequency ratio). As expected, lowering the number of laser shots limited the overall signal in the mass spectra (TIC) although the detected ions for both methods were comparable. The *m/z* peaks absent in the proposed method were the peaks that were already close to the limit of detection and isotope contributions. Interestingly, the absolute intensities of the minor ions were almost not affected compared to major ones when using fewer laser shots and 5 nmol/mm^2 of deposited matrix on mice's brain tissue sections. Table 2 reports the absolutes intensity, mass accuracy, and intensity ratio between major and minor lipids detected in the MS images of mice's brain tissue section when using 10 or 100 laser shots. The lipids were identified according to LIPID MAPS database peak annotation. Ions 772.53 *m/z* and 798.54 *m/z*

were the most intense signals observed while ions 770.51 *m/z* and 848.56 *m/z* are among the least intense ions in the mass spectrum. When comparing 10 to 100 laser shots, the intensities of minor ions were roughly halved while major ions intensities decrease by an order of magnitude. By reducing the number of laser shots per scan the relative intensities of the most intense ions tend to decrease to a larger extent in regards to the less intense ions. Any combination of intense/less intense ion ratios leads to the same observations. Besides, the intensity ratio between ions of comparable intensities (e.g. 772.53 m/z vs 798.54 m/z) was almost unaffected by the number of laser shot per scan.

Table 2. Intensities and ratio of detected and identified lipids in a mouse brain tissue section acquired with the MALDI FT-ICR-MS (solariX XR 9.4T) instrument for 10 and 100 laser shots

		10 shots				100 shots			
Target m/z	Identification	Intensity (c.p.s)	Mass accuracy (ppm)	Ratio m/z 772.53 over m/z target	Ratio m/z 798.54 over m/z target	Intensity (c.p.s)	Mass accuracy (ppm)	Ratio m/z 772.53 over m/z target	Ratio m/z 798.54 over m/z target
770.50975	$[PA\ 36:2+K]^+$	4.8E+05	-0.09	10.6	11.3	1.3E+06	-0.12	33.1	40.0
848.55643	$[PC\ 38:4+K]^+$	8.9E+05	-0.25	5.73	6.07	6.5E+06	-0.24	6.61	8.00
772.52519	$[PC\ 32:0+K]^+$	5.1E+06	-0.13		1.06	4.3E+07	-0.17		1.21
798.54079	$[PC\ 34:1+K]^+$	5.4E+06	-0.26	0.94		5.2E+07	-0.26	0.83	

The cause of the disparity in the ion intensity ratio when varying the number of laser shots to produce MS images was investigated. Indeed, it could be related to the ionization processes or due to the efficiency of the ion transmission by the ion optics and/or the MS analyzer (ICR cell). Similar experiments were conducted on a MALDI-ToF instrument (rapifleX, Bruker, Germany). Note that the rapifleX uses the Smartbeam 3D laser. To be somehow comparable with the Smartbeam II, the beamscan option was deactivated which avoids the laser energy being swept at the surface of the sample (i.e. matrix blaster). No variation of the ion intensity ratio was observed with the MALDI-ToF as shown in Table 3, despite we used a maximum of 1000 laser shots accumulation instead of 100, regardless of the major or minor ions considered. The ablated surface of the sample of only 25µm² with only 10 laser shots allowed the minor ions to still be detected and only matrix peaks intensities were strongly affected. The variation of the ion ratio observed with the MALDI FT-ICR was then related to the ion optics and/or the ICR mass analyzer. It is worth reminding that higher magnetic fields improve the dynamic range of the number of trapped ions inside the ICR in the absence of noticeable space charge effects.

Table 2. Intensities and ratio of detected and identified lipids in a mouse brain tissue section acquired with the MALDI ToF-MS (rapifleX) instrument (external calibration, enhanced cubic regression) for 10 and 1000 laser shots with the single focus option and without beamscan

		10 shots				1000 shots			
Target m/z	Identification	Intensity (c.p.s)	Mass accuracy (ppm)	Ratio m/z 782.57 over m/z target	Ratio m/z 798.54 over m/z target	Intensity (c.p.s)	Mass accuracy (ppm)	Ratio m/z 782.57 over m/z target	Ratio m/z 798.54 over m/z target
782.567	$[PC\ 36:4+H]^+$	6.8E+03	+9.7		0.79	1.8E+04	+7.1		0.81
798.541	$[PC\ 34:1+K]^+$	5.3E+03	+11.2	1.27		1.5E+04	+10.0	1.23	
806.567	$[PS\ 37:0+K]^+$	4.0E+03	-12.3	1.68	1.33	9.7E+03	-11.1	1.90	1.54
844.546	$[PC\ 36:3+Na]^+$	4.6E+03	+3.8	1.47	1.16	1.5E+04	6.2	1.22	0.99

3.6. Robustness of the mass spectrometry images at ultra-high mass resolving power using the MALDI FT-ICR solariX XR 9.4T. When applying the optimized method for extreme resolution MSI with an estimated R.P. over 500,000 at 800 *m/z* (>1'000'000 at m/z 400), a peak mass shift with much lower amplitude was observed and most importantly is fully within the instrument specifications, even in the average spectrum. The FWMH resolutions in individual spectra are now similar to the ones observed in the mean spectrum. The acquisition of such mass spectra quality during a mass spectrometry image experiment of rat brain samples was previously achieved using a custom prototype of a hybrid linear ion trap coupled to a 21T supra conducting magnet fitted with the dynamically harmonized cell (Paracell) by the NHMFL group at Tallahassee in Florida[37]. In this work, comparable results were obtained in terms of MSI mass resolving power and mass accuracies of mouse brain samples with a superconducting magnet of 9.4T using the same ICR cell (see Table S1). By comparing the mean spectrum of centroided MSI data performed on seriated brain slices (Figure 4a) and whole-body zebrafish slices (Figure 4b), the difference in image quality is clearly evident. The new method with controlled ion injection in the cell (TIC stabilized) resulted in narrow *m/z* peaks due to the restricted amplitude of the mass shift. The image of the ion distribution in the tissue section is also cleaner whether or not TIC or RMS normalization is applied (RMS not shown). To demonstrate the robustness of the controlled TIC method, replicates of brain seriated slices (roughly 12,000 pixels) and zebrafish whole body seriated slices (roughly 20,000 pixels) were acquired using our optimized method (Figure S5). In all cases, the experimental mass resolving power expected by the acquisition software was obtained. The imaging method was tested for images with FWMH resolution above 1,000,000 at 800 *m/z* on the brain of a zebrafish's whole-body slice

(roughly 1500 pixels). Figure S6 shows observable fine isotopic structures of intense ions directly in the mean spectrum further increasing the confidence of the identification process of these ions. Note that these images still show a slight loss of mass resolving power in the mean spectrum compared to individual pixels in agreement with the instrument specification of 0.5ppm at 800 *m/z* (*i.e.* 0.4 milli atomic mass unit). Clearly, the fine isotopic structure within a pixel of interest had improved mass resolving power. In complement, a peak realignment strategy by software post-processing coupled with our proposed MSI method of the mass spectrometry images was developed in our group to restore the isotopic fine structure also in the mean spectrum of average MS images having lower mass resolving power[38,39].

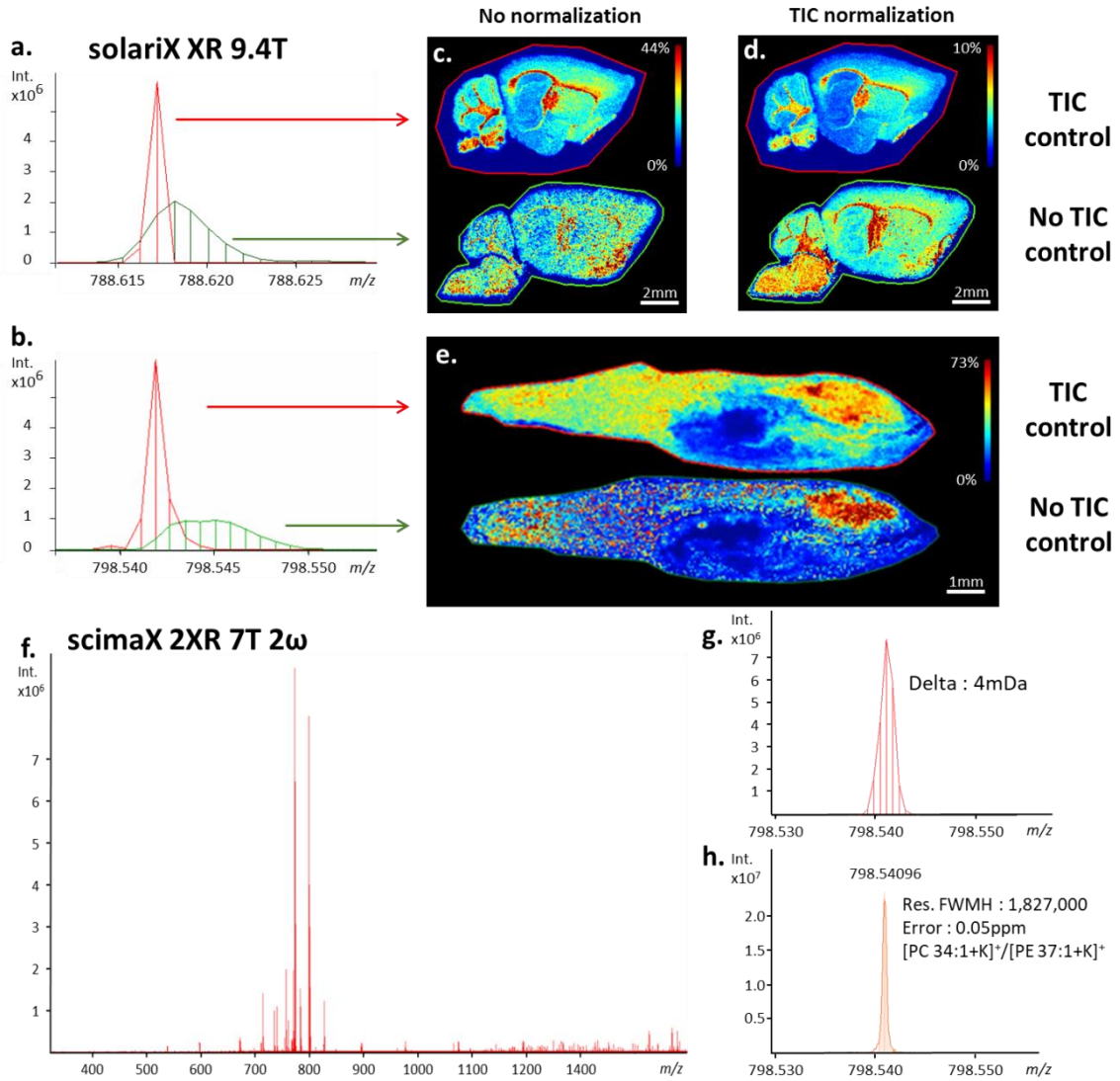

Figure 4. Averaged MSI mass spectra of MALDI-FT-ICR (solariX XR 9.4T, fitted with ParaCell) of mouse brain (a) and zebrafish (b), zoomed on peak 788,62 *m/z* and 798.54 *m/z* respectively, showing peak

width differences due to mass measurement accuracy obtained with (red) and without (green) the stabilization of the total ion current using optimization of the laser shot number (6 laser shots at 60 Hz). (c) reconstructed MS images using or not the TIC stabilization and without TIC normalization. (d) same as (c) but using a TIC normalization to reconstruct the MS images. (f) average mass spectrum of the mouse brain tissue section acquired on the scimaX 2XR using the 2ω detection mode. (g) averaged mass spectra focused on m/z 798.54 without TIC stabilization obtained on the scimaX 2XR 2ω, (h) averaged mass spectra focused on m/z 798.54 using the TIC stabilization method applied on the scimaX 2XR 2ω. See text for details.

3.7. Influence of the power of the magnetic field. FT-ICR operating at a high magnetic field (12T and above) are typically used for petroleomics analysis by direct infusion of diluted raw crude oils. Direct infusion (excluding any flowrate variation issues) allows for a stable TIC signal and fills the ICR cell with a constant number of ions at each scan. Higher magnetic fields allowed stable ion motion during long transient signal acquisition enabling very high mass resolving power. In addition, they allow the storage of a larger number of ions inside the ICR cells. Recently Ge and coworkers demonstrated the capability of FT-ICR operating at 7T and 2ω detection to closely match the performance of a 15T instrument for characterizing oil samples by direct electrospray infusion[40]. Mass spectrometry imaging takes also advantage of a higher magnetic field to produce higher quality mass spectrometry images [15,37]. In this work, the influence of TIC variation was investigated on FT-ICR equipped with a ParaCell but equipped with a lower magnetic field, i.e. 7T. The scimaX 2XR 7T instrument also provides the 2ω detection mode which recycles the excitation plates into detection plates to improve the duty cycle (transient signal) by a factor of 2 compared to the 1ω detection mode. Mice's brain MS images were compared for both 1ω and 2ω detection. Improved TIC stability, mass measurement accuracies, and spectral resolutions were obtained when using the optimized MSI method (See Figure 4f, 4g, 4h, and Figure S7). Interestingly, while no direct influence on ion current stability was observed when the 2ω detection mode was activated (Figure S8a), the mass shift was easier to constrain compared to 1ω mode datasets (Figure S8b). We assumed that the drastic diminution of the transient signal duration prevented peak coalescence as well as the decoherence of the ion packets inside the ICR cell[8,41]. It is worth mentioning that the comparison of MS images performed on seriated slices using 1ω and 2ω detection mode showed no tangible differences in terms of co-localization of the observed ions (Figure S8b). As an illustration, an MS image acquired with the solariX 9.4T and the scimaX 2XR 7T using the 2ω detection mode at 16M data points of 1000 pixels of mouse brain tissue section showed a resolution FWMH above 1,500,000 at 800 m/z and mass accuracy of 0.15ppm (Figure

4 f,g,h). The typical time to produce an image of 1000 pixels was 195 minutes using our solariX XR 9.4T (i.e. 1ω at 8M data point) and 205 minutes using the scimaX 2XR 7T operating at 2ω and 16M data point.

Table 4 shows the dynamic range obtained for major and minor lipids detected during the mass spectrometry imaging of 2 consecutive mice's brain tissue sections with the scimaX 2XR using 1 or 2ω detection mode. Note that the 7T instrument still required the ICR cell to be loaded with fewer ions than the 9.4T instrument using 1ω or 2ω detection to restrict the experimental mass shift in the average mass spectrum images. Therefore, fewer laser shots were used to produce the data in Table 4 compared to Tables 2 and 3. The ratios obtained for the scimaX 2XR using 1ω detection are somewhat similar to what we obtained with the solariX XR using the 9.4T superconducting magnet. The 2ω detection mode seems to be also beneficial because the dynamic range of the lipids detected in the mass spectrometry images was less affected than the 1ω detection mode. The higher power of the magnet is still beneficial for reaching a greater intra-scan dynamic range, or if the TIC cannot be efficiently stabilized even after optimizing the laser parameters. Nevertheless, MSI acquisition at extreme mass resolving power is possible using 7T superconducting magnet and 2ω detection.

Table 4. Intensities and ratio of detected and identified lipids in a mouse brain tissue section acquired with the MALDI FT-ICR-MS (scimaX 2XR 7T) instrument for 6 and 400 laser shots

		6 laser shots				400 laser shots			
Target m/z	Identification	Intensity (c.p.s)	Mass Accuracy (ppm)	Ratio *m/z* (a) over m/z target	Ratio *m/z* (b) over m/z target	Intensity (c.p.s)	Mass Accuracy (ppm)	Ratio *m/z* (a) over m/z target	Ratio *m/z* (b) over m/z target
scimaX 2XR 7T, 1ω detection mode									
713.45181	[PA 34:1+K]+	8.0E+5	+0.40	6.63	30.0	2.7E+6	+0.61	7.04	18.5
844.52531	[PC 38:6+K]+	2.4E+5	+0.53	22.1	100	Not detected	+0.58	N.D.	N.D.
772.52519	[PC 32:0+K]+	5.3E+6	+0,37		4.53	1.9E+7	+0.56		2.63
798.54079	[PC 34:1+K]+	2.4E+7	+0.26	0.22		5.0E+7	+0.44	0.38	
scimaX 2XR 7T, 2ω detection mode									
713.45181	[PA 34:1+K]+	4.3E+6	+0.23	3.72	4.88	4.9E+6	+0.40	4.29	10.4
844.52531	[PC 38:6+K]+	3.9E+6	+0.17	4.10	5.38	4.3E+6	+0.33	3.13	7.61
772.52519	[PC 32:0+K]+	1.6E+7	+0,22		1.31	2.1E+7	+0.37		2.43
798.54079	[PC 34:1+K]+	2.1E+7	+0.26	0.76		6.7E+7	+0.31	0.41	

m/z (a) corresponds to m/z 772,53 and *m/z* (b correspond to 798,54

N.D: not determined

3.8. Improvement of the mass peak annotation. Lastly, database queries for mass lists obtained with the optimized method showed an improvement in terms of peak annotations: fewer false positives and negatives were observed due to the improved mass resolving power, and mass accuracies could be achieved. Figure S9 shows some examples of database results as histograms of the matching counts at a given mass accuracy (in ppm) to detect readily any oddities in the dataset. When the TIC was not stabilized (not optimized method), most of the identifications had mass accuracy around -1.5 ppm. These values were not consistent with the specification of a properly calibrated FT-ICR and they do not fit with the requirement for proper annotation of lipids from the LIPID MAPS database. In contrast, the mass spectrometry image acquired with the optimized method and stabilized TIC led to a larger number of identifications, with scores around +0.4ppm that are well within the nominal performance for the instrument in terms of mass accuracy. The number of total matches is drastically improved due to fewer false-negative identifications and similarly, potentially fewer false-positive results. Of course, the addition of the fine isotopic structure further improves the confidence level of the identified lipids.

10.Conclusion

In this work, we successfully limited the space-charge effects and limited the resulting mass shift to improve the mass accuracy of MALDI mass spectrometry images of mouse brains and Zebrafish tissue sections by introducing a controlled TIC injection method in the ICR cell. The method was successfully applied on the solariX XR 9.4T and the scimaX 2XR 7T, two commercially available dual-source ESI/MALDI instruments fitted with the Paracell®. Under optimal instrumental settings, this was achieved primarily by optimizing the MALDI ion source lasers' parameters as well as the optimization of the deposited/sprayed amount of matrix. Mass spectrometry images with a resolving mass power better than 1,000,000 at 800 *m/z* were successfully produced in around 200 minutes for 1000 imaged pixels (transient duration of 11.7sec at 8M in the operated 300-1200 mass range using the common Amplitude mode for the solariX XR 9.4T, transient of 12.3 seconds for the scimaX 2XR 7T in 2ω detection mode at 16M data point) with no mass shift greater than 1 ppm range (typical mass shift below 0.5ppm) for the worst cases (around 0.5 milli atomic mass unit in the lipid mass range). The resulting images were also sharper at constant laser lateral resolution and matrix deposition method. Extreme resolution MS images obtained with relatively limited power of magnetic fields (below 12T) require a stabilized TIC throughout the MS image acquisition to retain the instrument specifications. The

intrascan dynamic range obtained during this work using the commercially available 9.4T and 7T instrument seemed to be around 100, while Bowman and coworker[37] reported a dynamic range of around 500 using a custom 21T MALDI FT-ICR instrument. Using 2ω detection on higher magnetic fields instrument will speed up the scan time by a factor of 2, allowing more samples to be imaged at constant mass resolving power during the same time frame. Peak annotations using the LIPID MAPS database correspond to scores better than 0.4 ppm, limiting misidentification of lipids detected in the images, especially when the extreme mass resolving power allows measurement of fine isotopic structure. Revisiting the laser parameters improved method reproducibility from pixels to pixels and also from sample-to-sample, which improved the robustness of our method by successfully performing similar mass spectrometry images of consecutive tissue sections in replicates.

It was found that the entrance voltage to the analyzer affects the number of ions introduced into the ICR cell in an interesting way that could potentially be used to limit the overflow of ions to be injected into the ICR cell, acting as an ion injection control device. The idea would be to limit ion current fluctuations in real-time for samples with high concentration heterogeneity of target compounds. This would require further investigation as it is currently considered a double-edged sword, as the signal can be easily lost if this voltage value is not properly set.

Acknowledgments

This work was supported by the Eurlipids Interreg V-A Euregio Meuse-Rhine with support from the European Fund for Regional Development of the European Union (www.eurlipids.com). This work was also a contribution to the EU Horizon 2020 research and Innovation program under grant agreement Nº 731077 and the European Project EU_FT-ICR_MS (H2020 INFRAIA-02-2017). The MALDI ToF rapifleX and the MALDI FT-ICR solariX XR were co-funded by FEDER BIOMED HUB Technology Support (number 2.2.1/996). All experiments were performed with permission from the Committee on Animal Welfare of Maastricht University and the Committee on Animal Welfare of Liege University, according to Dutch or Belgian governmental legislation, respectively.

References

(1) Le Rhun, E.; Duhamel, M.; Wisztorski, M.; Gimeno, J.-P.; Zairi, F.; Escande, F.; Reyns, N.; Kobeissy, F.; Maurage, C.-A.; Salzet, M.; Fournier, I. Evaluation of Non-Supervised MALDI Mass Spectrometry Imaging Combined with Microproteomics for Glioma Grade III Classification. *Biochimica et Biophysica*

Acta (BBA) - Proteins and Proteomics **2017**, *1865* (7), 875–890. https://doi.org/10.1016/j.bbapap.2016.11.012.

(2) Ellis, S. R.; Cappell, J.; Potočnik, N. O.; Balluff, B.; Hamaide, J.; Van der Linden, A.; Heeren, R. M. A. More from Less: High-Throughput Dual Polarity Lipid Imaging of Biological Tissues. *Analyst* **2016**, *141* (12), 3832–3841. https://doi.org/10.1039/C6AN00169F.

(3) Lamont, L.; Eijkel, G. B.; Jones, E. A.; Flinders, B.; Ellis, S. R.; Porta Siegel, T.; Heeren, R. M. A.; Vreeken, R. J. Targeted Drug and Metabolite Imaging: Desorption Electrospray Ionization Combined with Triple Quadrupole Mass Spectrometry. *Anal. Chem.* **2018**, *90* (22), 13229–13235. https://doi.org/10.1021/acs.analchem.8b03857.

(4) Wang, J.; Wang, C.; Han, X. Tutorial on Lipidomics. *Analytica Chimica Acta* **2019**, *1061*, 28–41. https://doi.org/10.1016/j.aca.2019.01.043.

(5) Marshall, A. G.; Hendrickson, C. L. High-Resolution Mass Spectrometers. *Annual Rev. Anal. Chem.* **2008**, *1* (1), 579–599. https://doi.org/10.1146/annurev.anchem.1.031207.112945.

(6) Kostyukevich, Y. I.; Vladimirov, G. N.; Nikolaev, E. N. Dynamically Harmonized FT-ICR Cell with Specially Shaped Electrodes for Compensation of Inhomogeneity of the Magnetic Field. Computer Simulations of the Electric Field and Ion Motion Dynamics. *J. Am. Soc. Mass Spectrom.* **2012**, *23* (12), 2198–2207. https://doi.org/10.1007/s13361-012-0480-1.

(7) Nikolaev, E. N.; Kostyukevich, Y. I.; Vladimirov, G. N. Fourier Transform Ion Cyclotron Resonance (FT ICR) Mass Spectrometry: Theory and Simulations: FT ICR MS. *Mass Spec Rev* **2016**, *35* (2), 219–258. https://doi.org/10.1002/mas.21422.

(8) Boldin, I. A.; Nikolaev, E. N. Fourier Transform Ion Cyclotron Resonance Cell with Dynamic Harmonization of the Electric Field in the Whole Volume by Shaping of the Excitation and Detection Electrode Assembly: New Principle of Ion Detection in a FTICR Penning Trap. *Rapid Commun. Mass Spectrom.* **2011**, *25* (1), 122–126. https://doi.org/10.1002/rcm.4838.

(9) Jertz, R.; Friedrich, J.; Kriete, C.; Nikolaev, E. N.; Baykut, G. Tracking the Magnetron Motion in FT-ICR Mass Spectrometry. *J. Am. Soc. Mass Spectrom.* **2015**, *26* (8), 1349–1366. https://doi.org/10.1007/s13361-015-1148-4.

(10) Popov, I. A.; Nagornov, K.; N.Vladimirov, G.; Kostyukevich, Y. I.; Nikolaev, E. N. Twelve Million Resolving Power on 4.7 T Fourier Transform Ion Cyclotron Resonance Instrument with Dynamically Harmonized Cell—Observation of Fine Structure in Peptide Mass Spectra. *J. Am. Soc. Mass Spectrom.* **2014**, *25* (5), 790–799. https://doi.org/10.1007/s13361-014-0846-7.

(11) Nikolaev, E. N.; Gorshkov, M. V.; Mordehai, A. V.; Talrose, V. L. Ion Cyclotron Resonance Signal-Detection at Multiples of the Cyclotron Frequency. *Rapid Commun. Mass Spectrom.* **1990**, *4* (5), 144–146. https://doi.org/10.1002/rcm.1290040503.

(12) Pan, Y.; Ridge, D. P.; Rockwood, A. L. Harmonic Signal Enhancement in Ion Cyclotron Resonance Mass Spectrometry Using Multiple Electrode Detection. *International Journal of Mass Spectrometry and Ion Processes* **1988**, *84* (3), 293–304. https://doi.org/10.1016/0168-1176(88)80106-X.

(13) Schweikhard, L. Theory of Quadrupole Detection Fourier Transform-Ion Cyclotron Resonance. *International Journal of Mass Spectrometry and Ion Processes* **1991**, *107* (2), 281–292. https://doi.org/10.1016/0168-1176(91)80064-T.

(14) Pan, Y.; Ridge, D. P.; Wronka, J.; Rockwood, A. L.; Marshall, A. G. Resolution Improvement by Using Harmonic Detection in an Ion Cyclotron Resonance Mass Spectrometer. *Rapid Commun. Mass Spectrom.* **1987**, *1* (7–8), 120–121. https://doi.org/10.1002/rcm.1290010709.

(15) Ferey, J.; Marguet, F.; Laquerrière, A.; Marret, S.; Schmitz-Afonso, I.; Bekri, S.; Afonso, C.; Tebani, A. A New Optimization Strategy for MALDI FTICR MS Tissue Analysis for Untargeted Metabolomics Using Experimental Design and Data Modeling. *Anal Bioanal Chem* **2019**, *411* (17), 3891–3903. https://doi.org/10.1007/s00216-019-01863-6.

(16) Longuespée, R.; Kriegsmann, K.; Cremer, M.; Zgorzelski, C.; Casadonte, R.; Kazdal, D.; Kriegsmann, J.; Weichert, W.; Schwamborn, K.; Fresnais, M.; Schirmacher, P.; Kriegsmann, M. In MALDI–Mass Spectrometry Imaging on Formalin-Fixed Paraffin-Embedded Tissue Specimen Section Thickness Significantly Influences *m/z* Peak Intensity. *Prot. Clin. Appl.* **2019**, *13* (1), 1800074. https://doi.org/10.1002/prca.201800074.

(17) Goodwin, R. J. A. Sample Preparation for Mass Spectrometry Imaging: Small Mistakes Can Lead to Big Consequences. *Journal of Proteomics* **2012**, *75* (16), 4893–4911. https://doi.org/10.1016/j.jprot.2012.04.012.

(18) Shimma, S.; Sugiura, Y. Effective Sample Preparations in Imaging Mass Spectrometry. *Mass*

Spectrometry **2014**, *3* (Special_Issue), S0029–S0029. https://doi.org/10.5702/massspectrometry.S0029.

(19) Morikawa-Ichinose, T.; Fujimura, Y.; Murayama, F.; Yamazaki, Y.; Yamamoto, T.; Wariishi, H.; Miura, D. Improvement of Sensitivity and Reproducibility for Imaging of Endogenous Metabolites by Matrix-Assisted Laser Desorption/Ionization-Mass Spectrometry. *J. Am. Soc. Mass Spectrom.* **2019**, *30* (8), 1512–1520. https://doi.org/10.1007/s13361-019-02221-7.

(20) Kaletaş, B. K.; van der Wiel, I. M.; Stauber, J.; Lennard J. Dekker; Güzel, C.; Kros, J. M.; Luider, T. M.; Heeren, R. M. A. Sample Preparation Issues for Tissue Imaging by Imaging MS: Sample Preparation Issues for Tissue Imaging. *Proteomics* **2009**, *9* (10), 2622–2633. https://doi.org/10.1002/pmic.200800364.

(21) Grassl, J.; Taylor, N. L.; Millar, Ah. Matrix-Assisted Laser Desorption/Ionisation Mass Spectrometry Imaging and Its Development for Plant Protein Imaging. *Plant Methods* **2011**, *7* (1), 21. https://doi.org/10.1186/1746-4811-7-21.

(22) Nishidate, M.; Hayashi, M.; Aikawa, H.; Tanaka, K.; Nakada, N.; Miura, S.; Ryu, S.; Higashi, T.; Ikarashi, Y.; Fujiwara, Y.; Hamada, A. Applications of MALDI Mass Spectrometry Imaging for Pharmacokinetic Studies during Drug Development. *Drug Metabolism and Pharmacokinetics* **2019**, *34* (4), 209–216. https://doi.org/10.1016/j.dmpk.2019.04.006.

(23) Prideaux, B.; Stoeckli, M. Mass Spectrometry Imaging for Drug Distribution Studies. *Journal of Proteomics* **2012**, *75* (16), 4999–5013. https://doi.org/10.1016/j.jprot.2012.07.028.

(24) Tressler, C.; Tilley, S.; Yang, E.; Donohue, C.; Barton, E.; Creissen, A.; Glunde, K. Factorial Design to Optimize Matrix Spraying Parameters for MALDI Mass Spectrometry Imaging. *J. Am. Soc. Mass Spectrom.* **2021**, *32* (12), 2728–2737. https://doi.org/10.1021/jasms.1c00081.

(25) Römpp, A.; Guenther, S.; Schober, Y.; Schulz, O.; Takats, Z.; Kummer, W.; Spengler, B. Histology by Mass Spectrometry: Label-Free Tissue Characterization Obtained from High-Accuracy Bioanalytical Imaging. *Angewandte Chemie International Edition* **2010**, *49* (22), 3834–3838. https://doi.org/10.1002/anie.200905559.

(26) Barry, J. A.; Robichaud, G.; Muddiman, D. C. Mass Recalibration of FT-ICR Mass Spectrometry Imaging Data Using the Average Frequency Shift of Ambient Ions. *J. Am. Soc. Mass Spectrom.* **2013**, *24* (7), 1137–1145. https://doi.org/10.1007/s13361-013-0659-0.

(27) Smith, D. F.; Kharchenko, A.; Konijnenburg, M.; Klinkert, I.; Paša-Tolić, L.; Heeren, R. M. A. Advanced Mass Calibration and Visualization for FT-ICR Mass Spectrometry Imaging. *J. Am. Soc. Mass Spectrom.* **2012**, *23* (11), 1865–1872. https://doi.org/10.1007/s13361-012-0464-1.

(28) Youmans, K. L.; Tai, L. M.; Nwabuisi-Heath, E.; Jungbauer, L.; Kanekiyo, T.; Gan, M.; Kim, J.; Eimer, W. A.; Estus, S.; Rebeck, G. W.; Weeber, E. J.; Bu, G.; Yu, C.; LaDu, M. J. APOE4-Specific Changes in Aβ Accumulation in a New Transgenic Mouse Model of Alzheimer Disease. *Journal of Biological Chemistry* **2012**, *287* (50), 41774–41786. https://doi.org/10.1074/jbc.M112.407957.

(29) Oakley, H.; Cole, S. L.; Logan, S.; Maus, E.; Shao, P.; Craft, J.; Guillozet-Bongaarts, A.; Ohno, M.; Disterhoft, J.; Van Eldik, L.; Berry, R.; Vassar, R. Intraneuronal Beta-Amyloid Aggregates, Neurodegeneration, and Neuron Loss in Transgenic Mice with Five Familial Alzheimer's Disease Mutations: Potential Factors in Amyloid Plaque Formation. *Journal of Neuroscience* **2006**, *26* (40), 10129–10140. https://doi.org/10.1523/JNEUROSCI.1202-06.2006.

(30) Sládková, K.; Houška, J.; Havel, J. Laser Desorption Ionization of Red Phosphorus Clusters and Their Use for Mass Calibration in Time-of-Flight Mass Spectrometry. *Rapid Commun. Mass Spectrom.* **2009**, *23* (19), 3114–3118. https://doi.org/10.1002/rcm.4230.

(31) Fahy, E.; Sud, M.; Cotter, D.; Subramaniam, S. LIPID MAPS Online Tools for Lipid Research. *Nucleic Acids Research* **2007**, *35* (Web Server), W606–W612. https://doi.org/10.1093/nar/gkm324.

(32) Sud, M.; Fahy, E.; Cotter, D.; Brown, A.; Dennis, E. A.; Glass, C. K.; Merrill, A. H.; Murphy, R. C.; Raetz, C. R. H.; Russell, D. W.; Subramaniam, S. LMSD: LIPID MAPS Structure Database. *Nucleic Acids Research* **2007**, *35* (Database), D527–D532. https://doi.org/10.1093/nar/gkl838.

(33) Fahy, E.; Subramaniam, S.; Brown, H. A.; Glass, C. K.; Merrill, A. H.; Murphy, R. C.; Raetz, C. R. H.; Russell, D. W.; Seyama, Y.; Shaw, W.; Shimizu, T.; Spener, F.; van Meer, G.; VanNieuwenhze, M. S.; White, S. H.; Witztum, J. L.; Dennis, E. A. A Comprehensive Classification System for Lipids. *Journal of Lipid Research* **2005**, *46* (5), 839–861. https://doi.org/10.1194/jlr.E400004-JLR200.

(34) Francl, T. J.; Sherman, M. G.; Hunter, R. L.; Locke, M. J.; Bowers, W. D.; McIver, R. T. Experimental Determination of the Effects of Space Charge on Ion Cyclotron Resonance Frequencies. *International Journal of Mass Spectrometry and Ion Processes* **1983**, *54* (1–2), 189–199.

https://doi.org/10.1016/0168-1176(83)85017-4.
(35) Easterling, M. L.; Mize, T. H.; Amster, I. J. Routine Part-per-Million Mass Accuracy for High- Mass Ions: Space-Charge Effects in MALDI FT-ICR. *Anal. Chem.* **1999**, *71* (3), 624–632. https://doi.org/10.1021/ac980690d.
(36) Veličković, D.; Zhang, G.; Bezbradica, D.; Bhattacharjee, A.; Paša-Tolić, L.; Sharma, K.; Alexandrov, T.; Anderton, C. R.; KPMP Consortium. Response Surface Methodology As a New Approach for Finding Optimal MALDI Matrix Spraying Parameters for Mass Spectrometry Imaging. *J. Am. Soc. Mass Spectrom.* **2020**, *31* (3), 508–516. https://doi.org/10.1021/jasms.9b00074.
(37) Bowman, A. P.; Blakney, G. T.; Hendrickson, C. L.; Ellis, S. R.; Heeren, R. M. A.; Smith, D. F. Ultra-High Mass Resolving Power, Mass Accuracy, and Dynamic Range MALDI Mass Spectrometry Imaging by 21-T FT-ICR MS. *Anal. Chem.* **2020**, *92* (4), 3133–3142. https://doi.org/10.1021/acs.analchem.9b04768.
(38) La Rocca, R.; Kune, C.; Tiquet, M.; Stuart, L.; Eppe, G.; Alexandrov, T.; De Pauw, E.; Quinton, L. Adaptive Pixel Mass Recalibration for Mass Spectrometry Imaging Based on Locally Endogenous Biological Signals. *Anal. Chem.* **2021**, *93* (8), 4066–4074. https://doi.org/10.1021/acs.analchem.0c05071.
(39) McCann, A.; Rappe, S.; La Rocca, R.; Tiquet, M.; Quinton, L.; Eppe, G.; Far, J.; De Pauw, E.; Kune, C. Mass Shift in Mass Spectrometry Imaging: Comprehensive Analysis and Practical Corrective Workflow. *Anal Bioanal Chem* **2021**, *413* (10), 2831–2844. https://doi.org/10.1007/s00216-021-03174-1.
(40) Ge, J.; Ma, C.; Qi, Y.; Wang, X.; Wang, W.; Hu, M.; Hu, Q.; Yi, Y.; Shi, D.; Yue, F.; Li, S.; Volmer, D. A. Quadrupole Detection FT-ICR Mass Spectrometry Offers Deep Profiling of Residue Oil: A Systematic Comparison of 2ω 7 Tesla versus 15 Tesla Instruments. *Analytical Science Advances* **2021**, *2* (5–6), 272–278. https://doi.org/10.1002/ansa.202000123.
(41) van Agthoven, M. A.; Lam, Y. P. Y.; O'Connor, P. B.; Rolando, C.; Delsuc, M.-A. Two-Dimensional Mass Spectrometry: New Perspectives for Tandem Mass Spectrometry. *Eur Biophys J* **2019**, *48* (3), 213–229. https://doi.org/10.1007/s00249-019-01348-5.

Supporting information

FTICR Mass spectrometry imaging at extreme mass resolving power using dynamically harmonized cell with 1ω or 2ω detection

Mathieu Tiquet[1], Raphaël La Rocca[1], Stefan Kirnbauer[3], Samuele Zoratto[3], Daan van Kruining[2], Loïc Quinton[1], Gauthier Eppe[1], Pilar Martinez-Martinez[2], Martina Marchetti-Deshmann[3], Edwin De Pauw[1], Johann Far[1]

[1] Mass Spectrometry Laboratory, MolSys Research Unit, University of Liège; Quartier Agora, Liège, Belgium
[2] Department of Psychiatry and Neuropsychology, School for Mental Health and Neuroscience, Maastricht University, Maastricht, the Netherlands
[3] Institute of Chemical Technologies and Analytics, TU Wien (Vienna University of Technology), Vienna, Austria

Figure S1. TIC vs time of a MALDI-FT-ICR acquisition where an increase of ions injected in the dynamically harmonized ICR cell is artificially induced around 3 minutes (a). Observable mass shift for m/z 753.61 between the mass spectra recorded before (blue, 10 laser shots per scan) and after (red, 400 laser shots per scan) the TIC increase shown in part (b).

Figure S2. Averaged MSI mass spectra of MALDI-FT-ICR (solariX XR 9.4T, fitted with ParaCell) of mouse brain highlighting the reduced presence of matrix ions when the amount of matrix sprayed is reduced from 10 (a) to 5 (b) nm/mm² of HCCA while laser parameters are switched from 400 shots with the minimum laser focus (a) to 6 shots with small laser focus setting (b).

Figure S3. Distribution of mass to charge ratio values (a) and FWMH resolution (b) found in the window 782.570 + 10mTh for the original acquisition method, i.e. 400 laser shots and 10nmol/mm² of sprayed matrix (left) and the optimized method, i.e. 6 laser shots and 5nmol/mm² of sprayed matrix (left) through entire MSI acquisition of mice's brain tissue sections (right).

Figure S5. Duplicate of two different sets of brain seriated slices (roughly 12,000 pixels) and a triplicate of zebrafish whole body seriated slices (roughly 20,000 pixels) acquired using our optimized method on our solariX MALDI FT-ICR-MS 9.4T demonstrating the robustness of our optimized MALDI MSI method.

Figure S6. Representation of the average mass spectrum of an extreme resolution 400 to 1200 m/z broadband MSI acquisition performed on a zebrafish brain accounting for 2000 pixels (up). Closes up on the different isotopes of the most intense ion where the isotopic fine structure is observed (middle). Image of the ion 798.5417 m/z distribution in the brain of a zebrafish (bottom left). Result from a database search in LIPID MAPS showing all matches with a 0.0005Th tolerance (bottom right).

Figure S6. Representation of the average mass spectrum of an extreme resolution 400 to 1200 m/z broadband MSI acquisition performed on a zebrafish brain accounting for 2000 pixels (up). Closes up on the different isotopes of the most intense ion where the isotopic fine structure is observed (middle). Image of the ion 798.5417 m/z distribution in the brain of a zebrafish (bottom left). Result from a database search in LIPID MAPS showing all matches with a 0.0005Th tolerance (bottom right).

Figure S 7. (a) Total Ion Count over time of mass spectrometry image acquisitions on a scimaX 2XR 7T in 1ω mode without controlling the ion current (red) and while controlling the ion current (green). (b) MS images mean spectra close up on the distribution of 798.54 m/z showing the limited mass shift obtained when using a method limiting TIC fluctuations (right) compared to a non-TIC controlling method (left).

Figure S 8. (a) Total Ion Count over time of mass spectrometry image acquisitions on a scimaX 2XR 7T in 1ω mode (orange) and 2ω mode (blue). (b) MS images mean spectra with the distribution of 772.53 m/z, 798.54 m/z, and 826.57 m/z with a close-up on 798.54 m/z to compare mass shift obtained with 1ω mode (right) and 2ω mode (left).

Figure S9 Representations of LIPID MAPS structure database (LMSD) bulk search results for peak lists as the number of matches versus their respective mass accuracy in ppm. MALDI dynamically harmonized FT-ICR MSI datasets shown were acquired with unstable Total Ion Count (A) and stabilized Total Ion Current (B).

Table S 1: figures of merit of MSI images produced on 7T, 9.4T, and 21T MALDI FT-ICR instruments fitted with the dynamically harmonized cell.

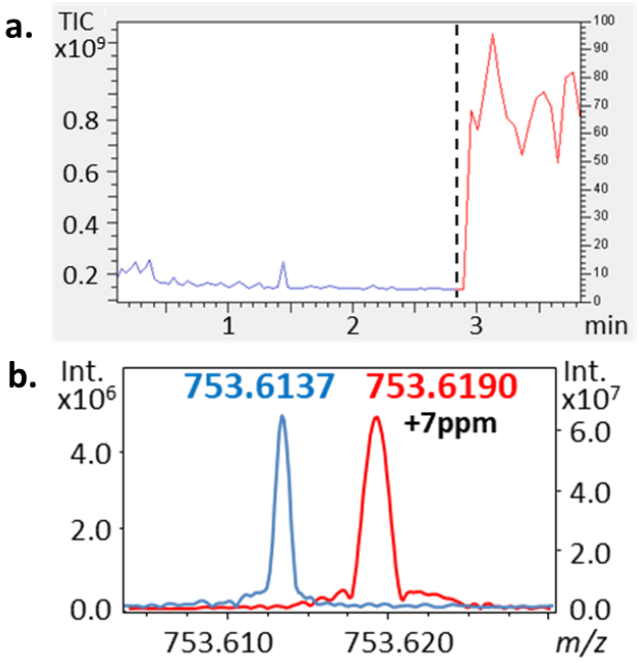

Figure S1. TIC vs time of a MALDI-FT-ICR acquisition where an increase of ions injected in the dynamically harmonized ICR cell is artificially induced around 3 minutes (a). Observable mass shift for m/z 753.61 between the mass spectra recorded before (blue, 10 laser shots per scan) and after (red, 400 laser shots per scan) the TIC increase shown in part (b).

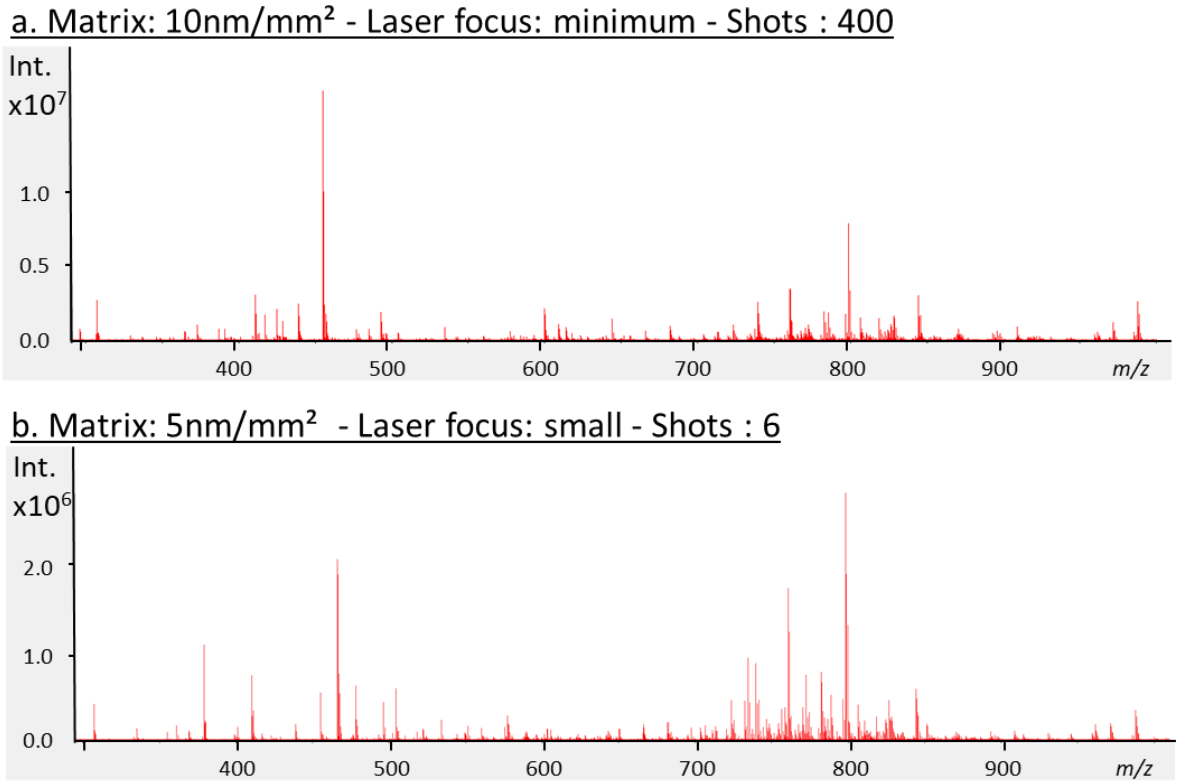

Figure S2. Averaged MSI mass spectra of MALDI-FT-ICR (solariX XR 9.4T, fitted with ParaCell) of mouse brain highlighting the reduced presence of matrix ions when the amount of matrix sprayed is reduced from 10 (a) to 5 (b) nm/mm² of HCCA while laser parameters are switched from 400 shots with the minimum laser focus (a) to 6 shots with small laser focus setting (b).

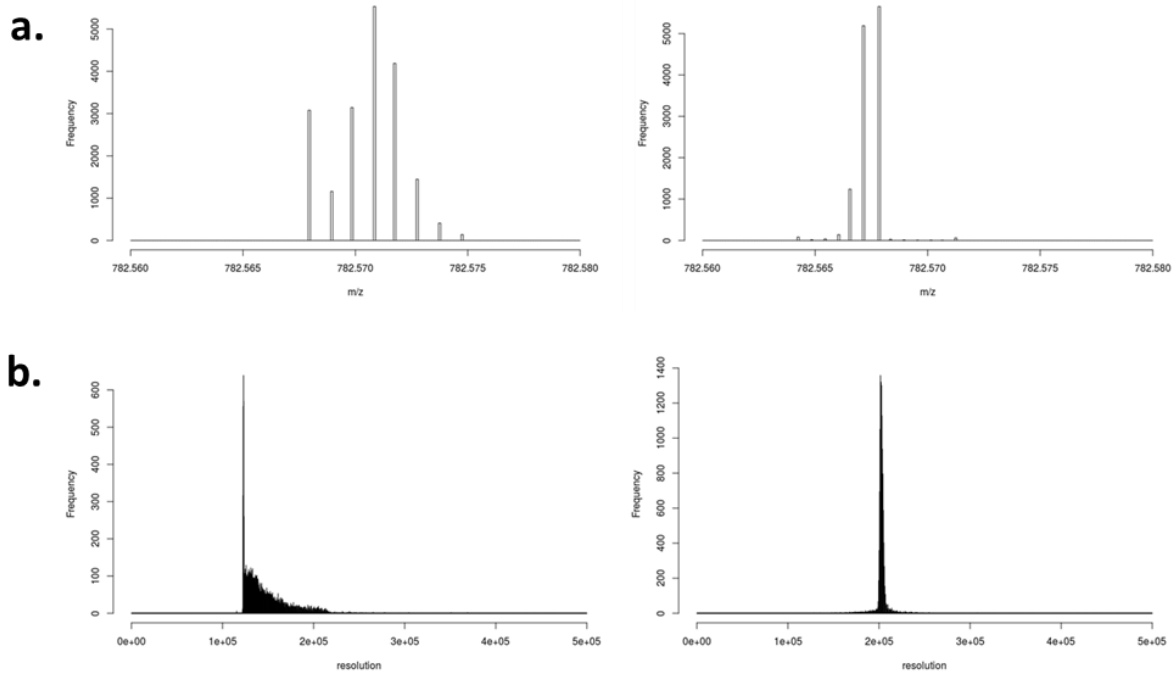

Figure S3. Distribution of mass to charge ratio values (a) and FWMH resolution (b) found in the window 782.570 + 10mTh for the original acquisition method, i.e. 400 laser shots and 10nmol/mm² of sprayed matrix (left) and the optimized method, i.e. 6 laser shots and 5nmol/mm² of sprayed matrix (left) through entire MSI acquisition of mice's brain tissue sections (right).

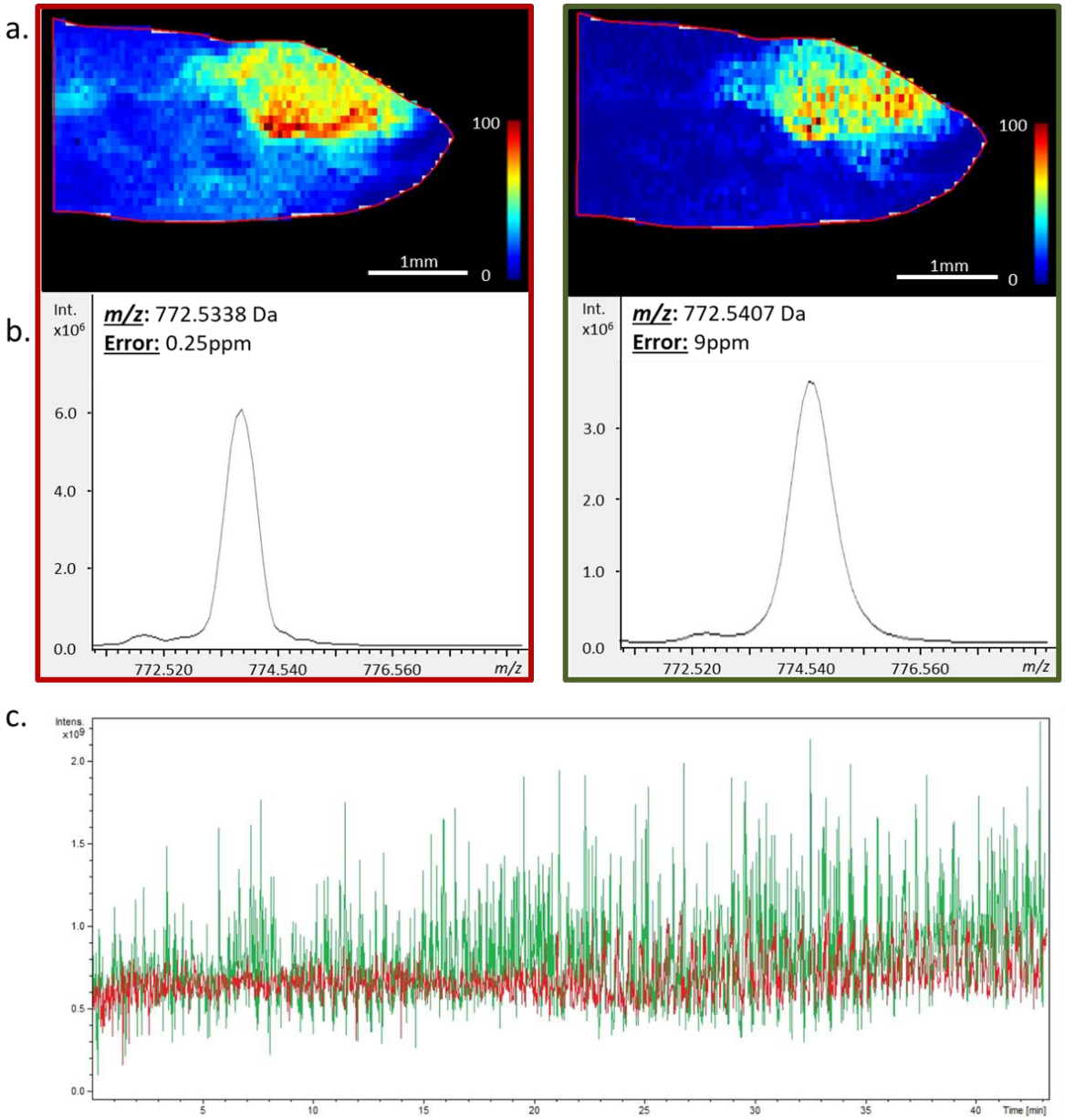

Figure S 4. (a) Localization of *m/z* 772.5338 in a pair intertwined MALDI-FT-ICR-MS images on a solariX 9.4T acquired with the manufacturer recommendations-based method (green) and lower amount of laser shots based method (red) performed on the same sagittal slice with an offset of 50µm on the x-axis for the second acquisition. (b) Close up on the corresponding peak in the mean spectrum of both images are provided in addition to the superposition of the Total Ion Current through MSI acquisitions (c).

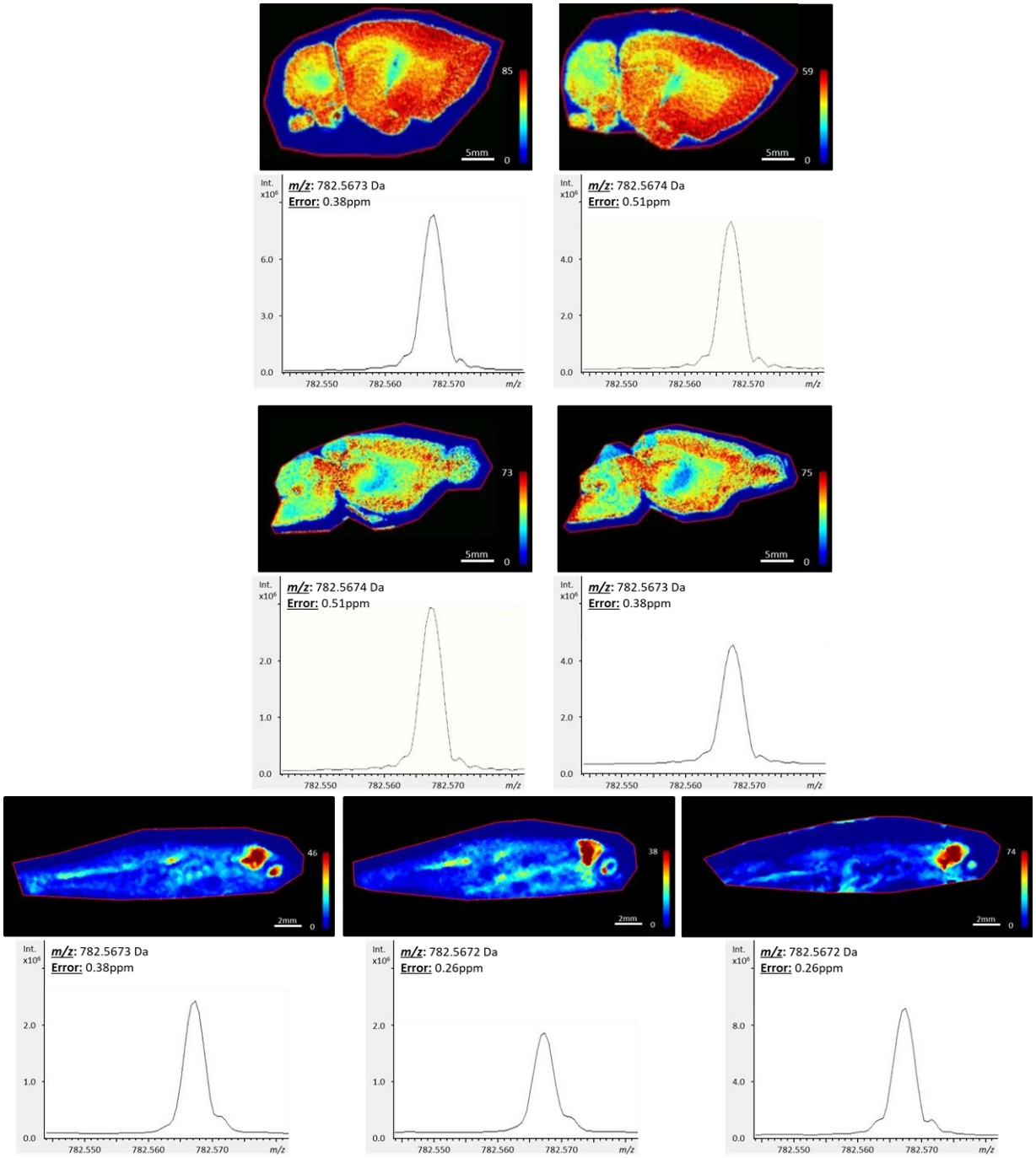

Figure S5. Duplicate of two different sets of brain seriated slices (roughly 12,000 pixels) and a triplicate of zebrafish whole body seriated slices (roughly 20,000 pixels) acquired using our optimized method on our solariX MALDI FT-ICR-MS 9.4T demonstrating the robustness of our optimized MALDI MSI method.

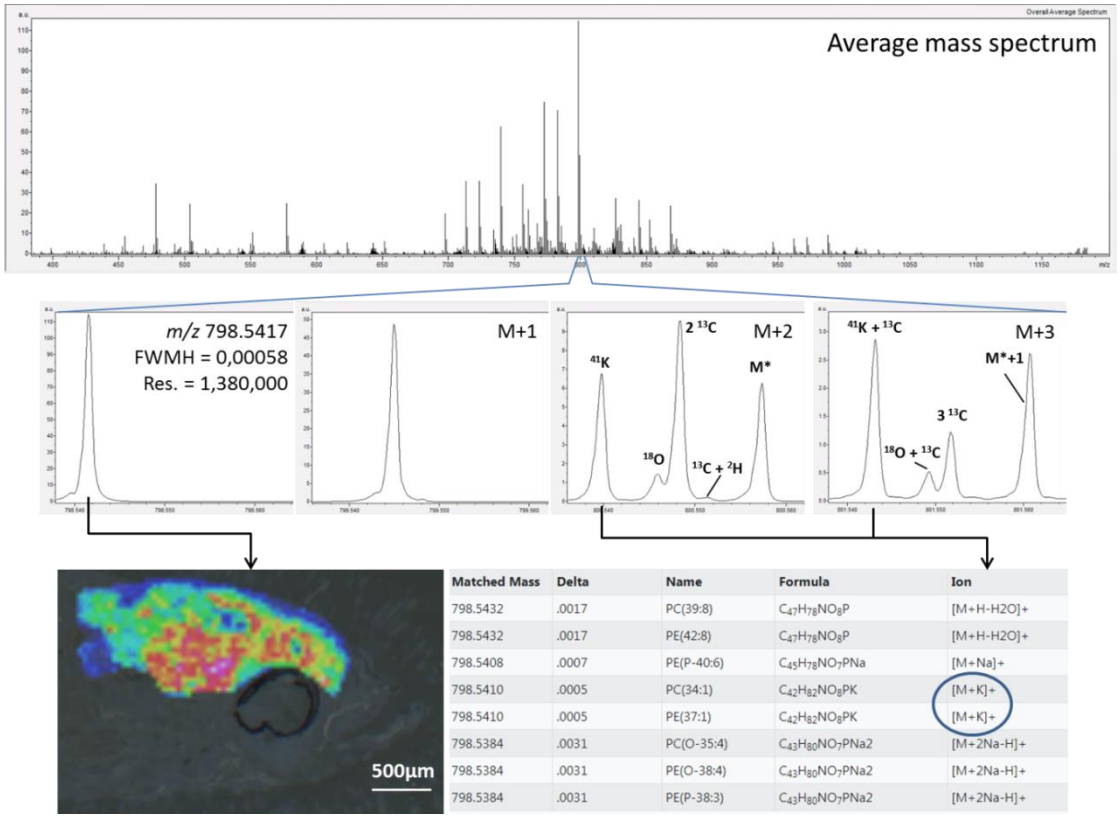

Matched Mass	Delta	Name	Formula	Ion
798.5432	.0017	PC(39:8)	$C_{47}H_{78}NO_8P$	[M+H-H2O]+
798.5432	.0017	PE(42:8)	$C_{47}H_{78}NO_8P$	[M+H-H2O]+
798.5408	.0007	PE(P-40:6)	$C_{45}H_{78}NO_7PNa$	[M+Na]+
798.5410	.0005	PC(34:1)	$C_{42}H_{82}NO_8PK$	[M+K]+
798.5410	.0005	PE(37:1)	$C_{42}H_{82}NO_8PK$	[M+K]+
798.5384	.0031	PC(O-35:4)	$C_{43}H_{80}NO_7PNa2$	[M+2Na-H]+
798.5384	.0031	PE(O-38:4)	$C_{43}H_{80}NO_7PNa2$	[M+2Na-H]+
798.5384	.0031	PE(P-38:3)	$C_{43}H_{80}NO_7PNa2$	[M+2Na-H]+

Figure S6. Representation of the average mass spectrum of an extreme resolution 400 to 1200 *m/z* broadband MSI acquisition performed on a zebrafish brain accounting for 2000 pixels (up). Closes up on the different isotopes of the most intense ion where the isotopic fine structure is observed (middle). Image of the ion 798.5417 *m/z* distribution in the brain of a zebrafish (bottom left). Result from a database search in LIPID MAPS showing all matches with a 0.0005Th tolerance (bottom right).

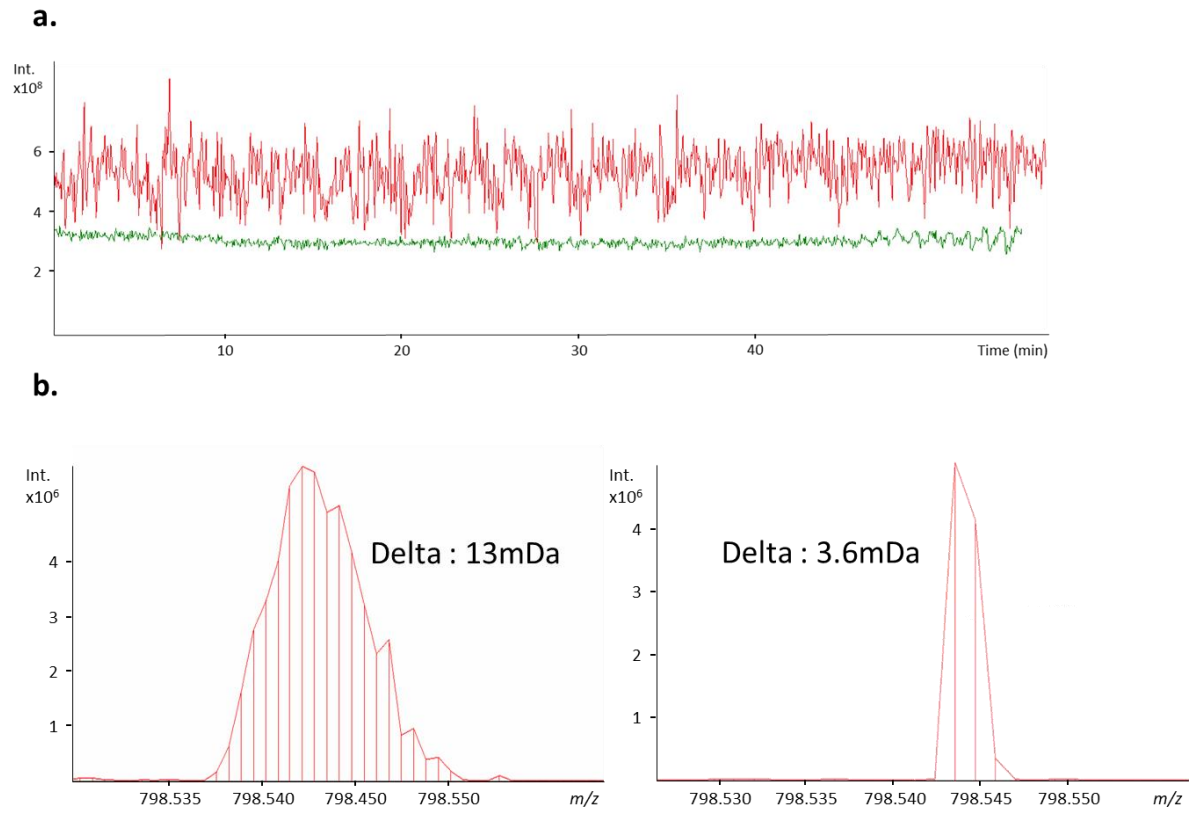

Figure S 7. (a) Total Ion Count over time of mass spectrometry image acquisitions on a scimaX 2XR 7T in 1ω mode without controlling the ion current (red) and while controlling the ion current (green). (b) MS images mean spectra close up on the distribution of 798.54 *m/z* showing the limited mass shift obtained when using a method limiting TIC fluctuations (right) compared to a non-TIC controlling method (left).

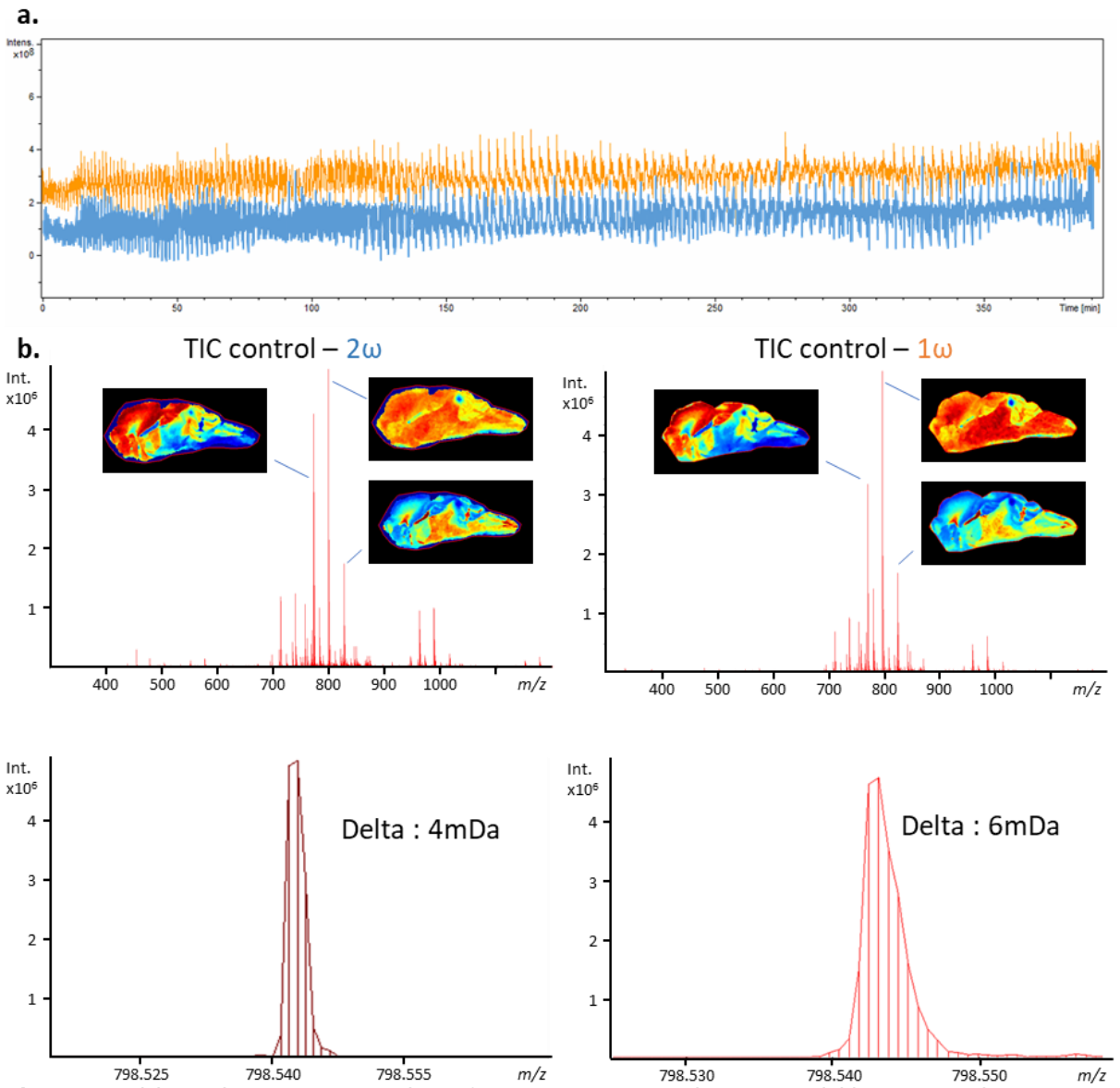

Figure S 8. (a) Total Ion Count over time of mass spectrometry image acquisitions on a scimaX 2XR 7T in 1ω mode (orange) and 2ω mode (blue). (b) MS images mean spectra with the distribution of 772.53 *m/*z, 798.54 *m/z*, and 826.57 *m/z* with a close-up on 798.54 *m/z* to compare mass shift obtained with 1ω mode (right) and 2ω mode (left).

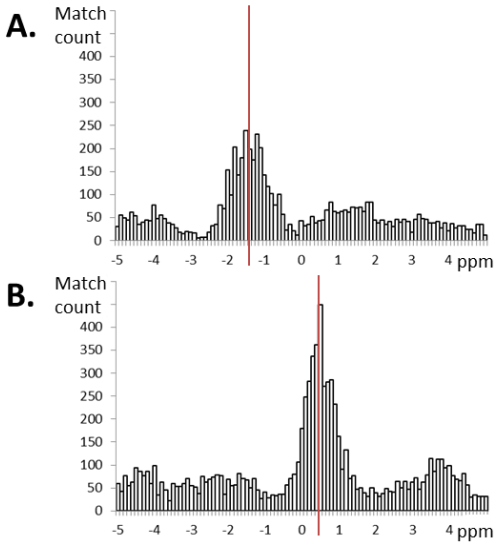

Figure S 9. Representations of LIPID MAPS structure database (LMSD) bulk search results for peak lists as the number of matches versus their respective mass accuracy in ppm. MALDI dynamically harmonized FT-ICR MSI datasets shown were acquired with unstable Total Ion Count (A) and stabilized Total Ion Current (B

Table S 1: figures of merit of MSI images produced on 7T, 9.4T, and 21T MALDI FT-ICR instruments fitted with the dynamically harmonized cell

Articles	Tiquet and coworkers		Bowman and coworkers*
MALDI MSI instrument	Commercial dual ESI/MALDI source ScimaX 2XR 7T	Commercial dual ESI/MALDI source solariX XR 9.4T	Prototype hybrid linear ion trap – 21T FT-ICR w/ Paracell (modified Velos pro linear ion trap from Thermo)
Processing mode	Amplitude mode	Amplitude mode	Absorption mode
Mass range	Broadband m/z 300 - 1200	Broadband m/z 300 - 1200	N.D. (assumed to be narrowband m/z 700-900)
Mass resolving power	> 1’500’000 on single spectrum @ m/z 800 @ 16M @ 2ω > 430’000 on average MSI @ 16M 1 or 2ω	> 400'000 @ m/z 800@ 4M on average MSI > 1'000'000 @m/z 800 @ 8M on average MSI	> 1'600'000 @ m/z 400 (i.e. > 800'000 @ m/z 800)
Mass calibration	External	External	Internal
Typical single spectra mass accuracy	< 0.2 ppm @ 2ω	< 0.5ppm	< 0.1ppm
Max. mass shift [a]	±1.2ppm (±1.0 mDa) [c]	±0.6ppm (±0.5 mDa)	N.D. (assumed to be around ±0.4ppm)
Dynamic range [b]	50-100	50-100	500
Transient duration	Around 12 sec @ 16M using 2ω detection	Around 12 sec @ 8M	Typical : 3.1sec

AGC	N.A.	N.A.	AGC disabled

* Bowman and coworkers, Anal. Chem. (2020),92 :3133-3142; DOI : 10.1021/acs.analchem.9b04768

N.A: Not applicable

a. Maximum mass shift experimentally obtained from *m/z* variation pixel-to-pixel in the whole mass spectrometry image. FWMH in the average MSI data were considered to define the mass deviation in mDa.

b. Intrascan dynamic range between the most intense identified lipid and the less intense identified lipids for the values reported by Tiquet and coworkers. For Bowman and coworkers, the dynamic range value is the one claimed by the author in their article.

c. Operating in extreme mass resolving power the scimaX 2XR 7T is more affected by limited TIC fluctuation due to the sample heterogeneity in regards to the solariX XR 9.4T and other FT-ICR using higher magnetic fields